Engineering Logical Inflammation Sensing and Secreting Circuit for Gut Modulation

Thesis by
Liana N. Merk

In Partial Fulfillment of the Requirements for the
Degree of
Bachelor of Science in Bioengineering

CALIFORNIA INSTITUTE OF TECHNOLOGY
Pasadena, California

2021
Defended June 1, 2021

Liana N. Merk
ORCID: 0000-0001-9711-954X

Abstract

The mammalian gut contains trillions of microbes that interact with host cells and monitor changes in the environment. Opportunistic pathogens exploit environmental conditions to stimulate their growth and virulence, leading to a resurgence of chronic disorders such as inflammatory bowel disease (IBD). Current therapies are effective in less than 30% of patients due to the lack of adherence to prescription schedules and overall, off-target effects. Microbial therapeutics can be engineered to colonize the gut, providing *in situ* surveillance and conditional disease modulation. However, many current engineered microbes can only respond to single gut environmental factors, limiting their effectiveness. In this work, we implement a previously characterized split activator AND logic gate in the probiotic *E. coli* strain Nissle 1917. Our system can respond to two input signals: the inflammatory biomarker tetrathionate and a second input signal, IPTG or aTC. We report 4-6 fold induction with minimal leak when both signals are present. We model the dynamics of the AND gate using chemical reaction networks, and by tuning parameters *in silico*, we identified perturbations that affect our circuit's selectivity. We then engineer our optimized AND gate to secrete an anti-inflammatory therapeutic cytokine, IL-22, using the hemolysin secretion pathway. We anticipate that our results will prove useful for designing living therapeutics for spatial targeting and signal processing in complex environments.

Contents

List of Figures

List of Tables

1 Introduction

Approximately 10^{13}–10^{14} bacterial cells live in the dynamic and complex community within the gut microbiome, where they can impact numerous facets of human health [1–3]. The idea that changes in the composition of this community result in disease offers a compelling motivation for engineering microbes to sense, modulate, or prevent these perturbations. Engineering microbes for gut diagnostics and therapeutics is a growing field in synthetic biology, owing to the tractability and relative safety of genome engineering in microbes. Recent examples include inhibition of pathogenic *Pseudomonas aeruginosa* via antimicrobial peptides [4] and delivery of checkpoint blockade nanobodies to tumors [5]. Due to the presence of bacteria in a wide variety of ecological niches, there exists a wide variety of evolved sensors for therapeutically-relevant molecules [6]. Microbes' ability to sense and respond to stimuli *in situ* offers controlled and targeted responses to traditionally difficult locations of disease.

One such complex microbiome perturbation is inflammation, which can drive dysbiosis, or disruptions in microbial populations [7]. Dysbiosis is a root cause of inflammatory bowel disease (IBD) and has been associated with infectious disease, obesity, and other medical disorders [8]. During IBD, specific niches within the gut microbiome change, causing spatial heterogeneity [9]. Currently, the most common treatment method for IBD is large doses of oral anti-inflammatory drugs, which have broad and nonspecific effects that do not account for the local environmental changes [10]. These anti-inflammatory drugs often require irregular and frequent dosage schedules challenging to adhere to, with the average patient missing half of their treatments [11].

Microbes capable of drug manufacture and secretion can colonize the microbiome, providing long-lasting *in situ* therapeutics without complex dosing schedules. Recent studies have found promise for inflammation treatment with microbes secreting interleukin-10 (IL-10) [12], IL-27 [13], and anti-tumor necrosis factor α [14].

In particular, a deficiency of IL-10 in mice is linked to a higher inflammatory response when challenged with pathogenic microbes [15]. Although IL-10 can be secreted and recognized by many cells in the immune system, its main anti-inflammatory response is known. IL-10 binds to the IL-10Rα and IL-10Rβ receptors, which activates a signal transducer pathway resulting in activation of transcription 3 (STAT3). This subsequently downregulates the T_H1-type and T_H2 cell responses. Several feedback loops exist to amplify and tune down the IL-10 pathway. Specifically, macrophages and dendritic cells can express IL-10 in response to pathogens through toll-like receptors (TLR) or non-TLR signalling [16]. Despite excitement surrounding IL-10's immunomodulatory potential, several clinical trials showed only a mild beneficial response in patient populations. One hypothesis is that only low concentrations of IL-10 are achieved at the site of inflammation. To combat this, *Lactococcus lactis* [17] and *Bifidobacterium bifidum* [18] have been engineered to express IL-10. These studies are ongoing, including an active clinical trial for *L. lactis* mediated delivery.

IL-22 is in the IL-10 cytokine family, but has slightly different physiological impacts. Whereas IL-10 downregulates inflammatory pathways through T cells and macrophages, IL-22 impacts regeneration and repair of tissue epithelial cell [19]. This decreases the proximity of pathogenic microbes to epithelial cells and mediates the surrounding inflammatory response to combat epithelial damage. IL-22 is recognized by the IL-22R1 and IL-10R2 re-

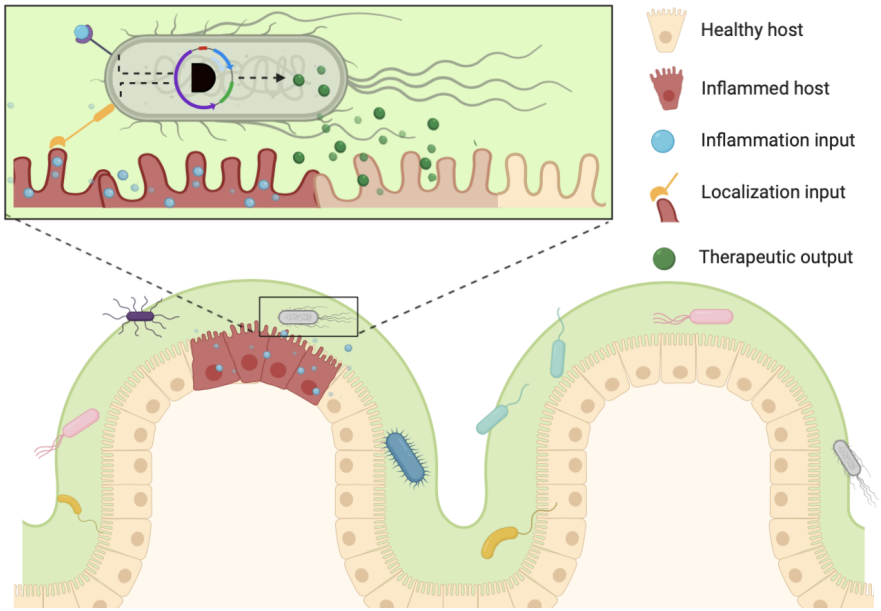

Figure 1: AND Gate Spatial Targeting. Production of the anti-inflammatory drug will only be active if cells detect that they are localized to the gut epithelium and the inflammation biomarker tetrathionate is present. Thus, anti-inflammatory action is only performed if the therapeutic cells are in the right place, minimizing off target effects. Figure not drawn to scale.

ceptors, which activate the JAK/STAT3, ERK, and JNK pathways. Like IL-10, the STAT3 pathway is responsible for most of IL-22's protective effects. Like IL-10, delivering IL-22 at the site of inflammation is of interest. Secretion via *Lactobacillus paracasei* has been shown to produce biologically active IL-22, but none of IL-22's ongoing clinical trials feature microbial delivery [20].

In the cases outlined here, engineered microbes express target molecules constitutively, not taking advantage of the ability of bacteria to sense and respond to their environment. This is especially relevant in IBD, a disease known to have spatial heterogeneity [7].

Genetic circuits responsive to inflammation are thus of great interest to the field of microbiome engineering. Two inflammatory biomarkers, nitric oxide [21] and tetrathionate [22] have been used as triggers for memory circuits, allowing for *in situ* inflammation diagnosis. The second biomarker, tetrathionate, has also been used to drive expression of microcins capable of inhibiting *Salmonella* spp. outgrowth [23]. Tetrathionate was first noted as a biomarker of intestinal inflammation by Winter et al. [24]. *Salmonella Typhimurium* was found to cause acute gut inflammation, causing the release of reactive oxygen species. These species react with intestinal sulfur compounds, most notably thiosulfates, causing the formation of a new respiratory electron acceptor, tetrathionate. *S. Typhimurium* and other pathogens, like *C. jejuni*, can gain a growth advantage by using tetrathionate as an electron acceptor.

Daeffler et al. identified a tetrathionate two-component sensor from the marine bacterium *Shewanella baltica* OS195 [6]. The system consists of a membrane-bound sensor

histidine kinase, ttrS, and a cytoplasmic response regulator, ttrR. Tetrathionate binds to ttrS, causing phosphorylation, leading to a complex that can phosphorylate ttrR. Phosphorylated ttrR, in turn, activates pTtr, which demonstrates low cross-activation by a range of other ligands likely present in the gut.

We implemented the hypersensitive response and pathogenicity (hrp) system reported by Wang et al. [25] to incorporate logical sensing. This system consists of two co-activating genes hrpR and hrpS that activate the σ54-dependent hrpL promoter [26]. The genetic elements were isolated from *Pseudomonas syringae* and optimized to function with various synthetic biology promoters, including pLac. Because the circuit is orthogonal to the *E. coli* genetic background, it can be engineered into *E. coli* Nissle without host genome interference. Here, we unite the inflammatory relevance of tetrathionate sensing with the regulatory control offered by this split activator system.

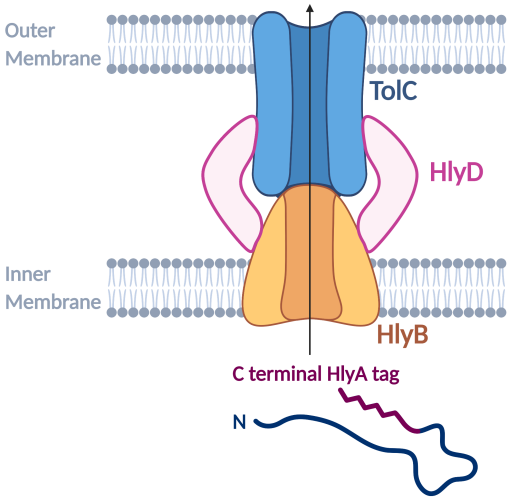

Figure 2: The HLY Secretion System. In inner membrane protein HlyB is connected to the outer membrane protein TolC by HlyD. The tagged protein's C-terminus enters the ATP-dependent HlyB protein and is secreted into the extracellular media in one step.

One challenge in engineering synthetic biology circuits to respond to human disease states is the potentially low concentration capacity offered by microbes. In fact, many molecules destined for human use are engineered in the large gram-positive bacterium *Bacillus megaterium* [27]. However, the genetic tractability and microbiota colonization studies in *E. coli* motivate exploration of increasing therapeutic molecule concentration in the extracellular environment. Specifically, much research has focused on using the native protein secretion machinery for recombinant proteins. *E. coli* secretions are diverse, with two main types of mechanisms [28]. First, one-step pathways directly transport proteins from the cytoplasm to extracellular media or target cells. Applications of one-step transport include secretion of proteins, proteases, and adhesins to the surrounding environment through type 1 secretion systems (T1SS). *E. coli* are also able to transport DNA (T3SS) and effector proteins (T4SS) to adjacent cells. The second type of transport occurs in two steps, with the

first transport into the periplasm across the inner membrane, and the second occurring across the outer membrane. Examples of this mechanism include T2SS, which is natively used to excrete exoenzymes, toxins, and adhesins. T5SS and T7SS are involved in biofilm formation and curli secretion, respectively. All of the mechanisms mentioned here are ATP-dependent and thus have an effect on the cell's energetic reserves.

In terms of engineering applications, type 1 secretion systems have been extensively pursued due to their efficiency and broad range of naturally secreted substrates ranging from heme-binding proteins to toxins. One of the most well-studied type 1 secretion systems, HlyA, was derived from uropathogenic *E. coli* strains and has been implemented in nonpathogenic laboratory strains. Other engineered secretion systems, like TliCDEF, function optimally at 25°C, which is not optimal for gut applications [29]. Thus, the hemolysin secretion system is an attractive choice. This system consists of three membrane proteins: the ATP-binding translocator HlyB, the outer membrane protein TolC, and the membrane fusion protein HlyD that connects HlyB to TolC. The two hemolysin secretion-derived proteins, hlyB and hlyD, are not endogenous to Nissle, while TolC is present on the *E. coli* genome.

The hlyB-hlyD-TolC channel can export proteins that are tagged with 600 bp of the C terminal hlyA sequence. Successful secretion pursuits include active *E. coli* β-galactosidase [30], *Thermobifida fusca* cutinase [31], and GFP [32]. It is thought that the transporter rate is approximately 16 amino acids per transporter per second. This rate is independent of substrate size and extracellular calcium ion concentration [33]. However, the rate of folding of the substrate does play a role in secretion rate [34].

Relevant to the field of gut engineering, this secretion pathway has been used to secrete single domain antibodies complementary to enterohemorrhagic *E. coli* antigens [35] and mammalian intestinal fatty acid-binding protein [36]. In Nissle, two notable applications of the hemolysin pathway are noted: secretion of mouse IL-10 [37] and an HIV fusion inhibitor peptide [38]. However, these applications have relied on either constitutive or isopropylthiogalactoside (IPTG) activated expression, and do not link environmental sensing to therapeutic output.

While microbes have been engineered to respond to environmental factors like inflammation, they are often limited to sensing single inputs. The complexity of the gut environment necessitates engineering of systems that may respond to a wide array of conditions. Further, as the microbiome field moves towards engineering microbial consortia, the ability to multiplex several logic gates provides a unique ability to coordinate cross-species responses to a set of inputs. Here, a previously characterized split activator AND logic gate was used to trigger selective activation to inflammatory biomarker tetrathionate and IPTG [25]. To guide choices of genetic elements, a mathematical model of the tetrathionate two-component system was used. Optimization of the validated tetrathionate system was then performed in the context of the split activator AND gate in *E. coli* Nissle. This system consists of a two plasmid construct that responds selectively to IPTG and tetrathionate. To explore leak and points towards potential improvements in the circuit design, a chemical reaction network describing all reactions in the AND gate system was built. Towards the goal of therapeutically relevant output molecules, the HlyA secretion system was optimized in *E. coli* Nissle through plate-based and *in vitro* assays.

2 Results

2.1 Modeling the Tetrathionate Two-Component System

To validate the experimental optimization steps, we built a mathematical model by writing the chemical reactions that describe the dynamics of the two-component system. Two component signaling is one of the most prevalent methods that microbes gene expression from transmembrane signals [39]. To understand the effects of various experimental tuning steps such as the ribosome binding strength on the expected output, we describe a model for the tetrathionate signaling system. This model is divided into three parts — the expression of tetrathionate regulators ttrS and ttrR, phosphorylation of the tetrathionate regulators, and the reporter gene's activation. Table 1 describes the two-component system model in detail. The notation x:y denotes a complex between the chemical species x and y. Moreover, all binding rates are denoted with a "b" superscript, and unbinding reactions are denoted with a "u" superscript. A superscript P denotes phosphorylated species and an asterisk superscript is used to denote activated form of a species. Parameter values can be found in Table 2. All code to regenerate the simulations is publicly available on GitHub [40].

The regulator's constitutive expression, ttrS and ttrR are under the common promoter J23103 (P1d) [41]. Since these parts are co-transcribed, we model a single transcription reaction for both regulators. Transcription is modeled as a two-step process: binding the promoter to the RNA polymerase to form a complex and transcription of the complex to the corresponding mRNAs. Since each regulator is under control of its own ribosome binding site, we have modeled two separate translation reactions. The translation is also modeled as a two-step process where a ribosome binds to the mRNA transcript to form a complex that then translates to express the regulator protein.

For the phosphorylation pathway, we model the tetrathionate molecule binding to ttrS as reversibly triggering phosphorylation. The cytoplasmic response protein ttrR can bind to either the phosphorylated or dephosphorylated ttrS. If ttrR binds to dephosphorylated ttrS, there is a higher OFF rate than if ttrR binds to phosphorylated ttrS. Phosphorylation of ttrR only occurs once it binds to the phosphorylated ttrS forming a complex, ttrR:ttrS$^{\mathrm{P}}$. It is not known whether the dephosphorylation of ttrR is phosphatase dependent, like the KdpD/KdpE TCS in *E. coli* [42]. Here, we do not model phosphatase explicitly but rather set an explicit rate, k_{dephos}, that defines the dephosphorylation of ttrR.

The third and final part of the two-component signaling model is the activation of the GFP reporter gene. Phosphorylated ttrR may dimerize reversibly within the cytoplasm. It is not known whether inactive ttrR (that is, dephosphorylated dimers or monomers) can bind to the promoter region. Here, we only model the dimerized, phosphorylated ttrR as activators of gene expression. Once the activated ttrR binds, the inactive pTtr promoter is converted to an active state, denoted as pTtr*. RNA polymerase may only bind to this activated promoter. This triggers the transcription of the GFP transcript, GFP$_{\mathrm{T}}$. This transcript then binds reversibly with a ribosome and is irreversibly converted into the unbound ribosome, GFP$_{\mathrm{T}}$, and GFP protein.

Choosing reaction rate parameter values for the different chemical reactions is a critical step in modeling the signaling system. Since finding exact values for all the rate parameters *a priori* is impossible, we make a few simplifying assumptions. We assume that the explicit

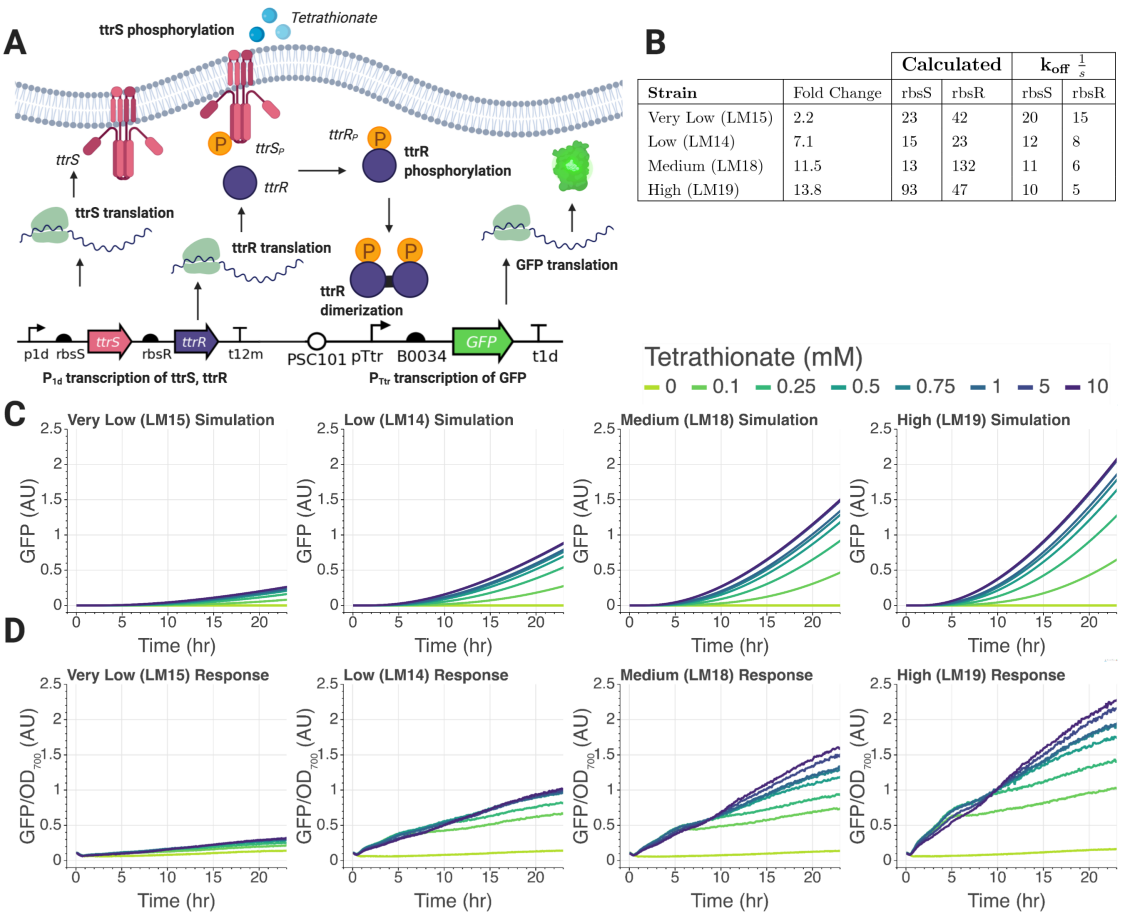

		Calculated		k_{off} $\frac{1}{s}$	
Strain	Fold Change	rbsS	rbsR	rbsS	rbsR
Very Low (LM15)	2.2	23	42	20	15
Low (LM14)	7.1	15	23	12	8
Medium (LM18)	11.5	13	132	11	6
High (LM19)	13.8	93	47	10	5

Figure 3: Expression and Simulation of Tetrathionate Response Circuit. A. Schematic of tetrathionate two component system. All shown steps were modeled using chemical reaction networks. **B.** Relative RBS binding strengths to ttrS and ttrR calculated from sequenced RBS sites isolated from 4 functioning tetrathionate response circuits. Off rates for simulated reactions. **C.** Simulations of RBS tuning by varying ribosome off rates to each ribosome binding sites. **D.** Plate reader time course with increasing tetrathionate concentrations and different ribosome binding strengths.

translation rates are identical for all mRNAs in the system. Further, we also assume that all degradation reactions occur at the same rate. We selected the nominal values from the various results and information available in the literature, discussed further in Table 2. Since the ribosome binding strength is a tunable parameter in the experimental design, we keep this parameter free to change during the simulations to observe its effects. The different RBS strengths are modeled by changing the ribosome's unbinding reaction rates to a given transcript.

The model simulations with varying ribosome binding strengths are shown in Figure 3-C. The model predicts that the RBS preceding the inducers has a strong effect on output fold change. With increasing ribosome binding strengths, the model simulations show an

increased fold change and higher reporter protein expression. The experimental results seem to show a similar performance with changing RBS strength, as shown in Figure 3-D. We used a Python toolbox called BioCRNpyler [45] to generate the model and ran simulations using the Bioscrape [46] simulator. The Python code used to generate the simulations shown in Figure 3-C is available publicly on GitHub [40].

A future line of work would be to quantitatively validate the model parameters by fitting

Table 1: The Two-Component System Model

Description	Reaction
Transcription and Translation of Regulators	
RNA Polymerase binds to P1d	$P + P1d \underset{k_1^u}{\overset{k_1^b}{\rightleftharpoons}} P1d{:}P$
Transcription of ttrS, ttrR	$P1d{:}P \xrightarrow{k_{tx}} ttrS_T + ttrR_T + P1d + P$
Translation $ttrS_T$ to ttrS	$ttrS_T + R \underset{k_2^u}{\overset{k_2^b}{\rightleftharpoons}} ttrS_T{:}R \xrightarrow{k_{tl}} ttrS_T + R + ttrS$
Translation $ttrR_T$ to ttrR	$ttrR_T + R \underset{k_3^u}{\overset{k_3^b}{\rightleftharpoons}} ttrR_T{:}R \xrightarrow{k_{tl}} ttrR_T + R + ttrR$
Tetrathionate Regulator Phosphorylation Pathway	
Tetrathionate (tt) triggering ttrS phosphorylation	$ttrS + tt \underset{k_4^u}{\overset{k_4^b}{\rightleftharpoons}} ttrS^P + tt$
ttrR binding to unphosphorylated ttrS	$ttrR + ttrS \underset{k_5^u}{\overset{k_5^b}{\rightleftharpoons}} ttrR{:}ttrS$
ttrR binding to phosphorylated ttrS	$ttrR + ttrS^P \underset{k_6^u}{\overset{k_6^b}{\rightleftharpoons}} ttrR{:}ttrS^P$
Phosphorylation of ttrR	$ttrR{:}ttrS^P \underset{k_7^u}{\overset{k_7^b}{\rightleftharpoons}} ttrR^P + ttrS$
Dephosphorylation of ttrR	$ttrR^P \xrightarrow{k_{dephos}} ttrR$
Response Regulator Gene Activation	
Dimerization of $ttrR^P$	$ttrR^P + ttrR^P \underset{k_8^u}{\overset{k_8^b}{\rightleftharpoons}} ttrR_2^P$
$ttrR^P$dimer binding to pTtr promoter	$ttrR^P + pTtr \underset{k_9^u}{\overset{k_9^b}{\rightleftharpoons}} pTtr^*$
RNA Polymerase binds to $pTtr^*$	$P + pTtr^* \underset{k_{10}^u}{\overset{k_{10}^b}{\rightleftharpoons}} pTtr^*{:}P$
GFP Transcription	$pTtr^*{:}P \xrightarrow{k_{tx}} pTtr^* + P + GFP_T$
GFP Translation	$GFP_T + R \underset{k_{11}^u}{\overset{k_{11}^b}{\rightleftharpoons}} GFP_T{:}R \xrightarrow{k_{tl}} GFP_T + R + GFP$
Degradation Reactions	
$ttrS_T$ and ttrS degradation	$ttrS_T \xrightarrow{\delta} \varnothing$ $\quad$ $ttrS \xrightarrow{\delta} \varnothing$
$ttrR_T$ and ttrR degradation	$ttrR_T \xrightarrow{\delta} \varnothing$ $\quad$ $ttrR \xrightarrow{\delta} \varnothing$
GFP_T and GFP degradation	$GFP_T \xrightarrow{\delta} \varnothing$ $\quad$ $GFP \xrightarrow{\delta} \varnothing$

Table 2: Model Parameters

S.no.	Param.	Description	Guess	Ref.
1	k_{tx}	Transcription rate (transcripts/second)	0.1	Guess
2	k_{tl}	Translation rate	1	Guess
3	k_{dephos}	Dephosphorylation rate	50	[43]
4	k_1^b	Binding of RNA polymerase to P1d	10	[44]
5	k_1^u	Unbinding of RNA polymerase and P1d complex	0.0001	[44]
6	k_2^b	Binding of ttrS transcript to its ribosome	0.3	[43]
7	k_2^u	Unbinding of ttrS and ribosome complex	Varies	Guess
8	k_3^b	Binding of ttrR transcript to its ribosome	0.3	[43]
9	k_3^u	Unbinding of ttrR and ribosome complex	Varies	Guess
10	k_4^b	Binding of tetrathionate to ttrS	1.6	[43]
11	k_4^u	Unbinding of tetrathionate and ttrS complex	0.016	[43]
12	k_5^b	Binding of ttrR to ttrS	0.0001	[43]
13	k_5^u	Unbinding of ttrR and ttrS complex	6	Guess
14	k_6^b	Binding of ttrR to phosphorylated ttrS	0.0001	[43]
15	k_6^u	Unbinding of ttrR and ttrS^{P} complex	1	Guess
16	k_7^b	Forward rate for phosphorylation of ttrR	1	[43]
17	k_7^u	Reverse rate for phosphorylation of ttrR	1	[43]
18	k_8^b	Dimerization rate of phosphorylated ttrR	0.0083	[43]
19	k_8^u	Unbinding of the dimerized complex of phosphorylated ttrR	0.5	[43]
20	k_9^b	Forward rate of activation of pTtr promoter	0.3	[43]
21	k_9^u	Reverse rate of activation of pTtr promoter	0.0001	Guess
22	k_{10}^b	Binding of RNA polymerase to activated pTtr promoter	10	[44]
23	k_{10}^u	Unbinding of RNA polymerase and activated pTtr promoter complex	0.0001	[44]
24	k_{11}^b	Binding of GFP transcript to its ribosome	100	Guess
25	k_{11}^u	Unbinding of GFP transcript and ribosome complex	10	Guess

the experimental data to the simulations so that the model can be used to make credible predictions. Since various parameters in the model are context-dependent, parameter tuning of a validated model *in silico* may provide helpful insights when implementing this circuit in the gut environment. Similarly, the effects of resource sharing and high burden due to the expression of proteins may be quantified using this model. Towards that end, we discuss the results from preliminary data collected for the two component system in the next section.

2.2 Tetrathionate Sensor Validation

The end goal of our construct is implementation into the microbiome. As such, we wanted to minimize the number of plasmid constructs present in our system. We designed a single construct to have all regulators as well as the tetrathionate inducible promoter, pTtr, shown in Figure 3-A. We engineered the inducible promoter after the regulators, which are constitutively expressed. Thus, if the polymerase reads through the regulator terminator, it would not express the pTtr construct.

Using 3G assembly [47], we constructed a tetrathionate-responsive circuit. To minimize leak while maximizing circuit response, we screened regulators of varying expression strengths. We optimized the RBS preceding both tetrathionate sensing regulators ttrS and ttrR using the Andersen RBS pool [41]. We transformed constructs into JM109 *E. coli* strain and selected six constructs for sequencing. We estimated the RBS strengths of the sequenced circuit constructs shown in Figure 4-B [48]. Weak RBS preceding ttrS or ttrR leads to a lower fold change of GFP expression upon the addition of tetrathionate, as seen in the simulated results as well. The high activation circuit, LM19, was selected for the next steps due to 13.8x activation with maximum tetrathionate input.

2.3 Engineering Two-Input AND Gate

To incorporate logical sensing, we chose a system of co-dependent split activators to drive expression of our reporter gene. One regulator, hrpR, is driven by the tetrathionate-dependent promoter. The second regulator, hrpS, is driven by pLac, which activates in the presence of IPTG. These two regulators form a homo-hexameric complex needed to activate pHrpL, which drives GFP expression, shown in Figure 4-A. Our circuit should thus only activate in the presence of tetrathionate and IPTG, shown in the truth table in Figure 4-B.

While this split activator system has previously been tested in seven different chassis [25], it has not been tested in *E. coli* Nissle 1917. We first performed one round of optimization of the AND gate components in *E. coli* Marionette Clo cells [49] which natively express lacI. Initially, the RBS reported by Wang et al. [25] were used, with B0034 for hrpR and rbsH for hrpS. However, expression was leaky in all inducer conditions, suggesting that the activator expression might be too high. To resolve this, we cloned the Anderson library of ribosome binding sites (ARL) [41] in front of hrpR. We then isolated five constructs with significant fold change in response to both inducers — IPTG and tetrathionate. Constructs were isolated, sequence verified, and re-transformed into Nissle, shown in Figure 4-D.

To optimize this system in *E. coli* Nissle, we found proper expression level of lacI such that pLac can be regulated. We co-transformed a constitutively expressed lacI and mScarlet plasmid with the working AND gate plasmid optimized in Marionette Clo. Using stereoscope

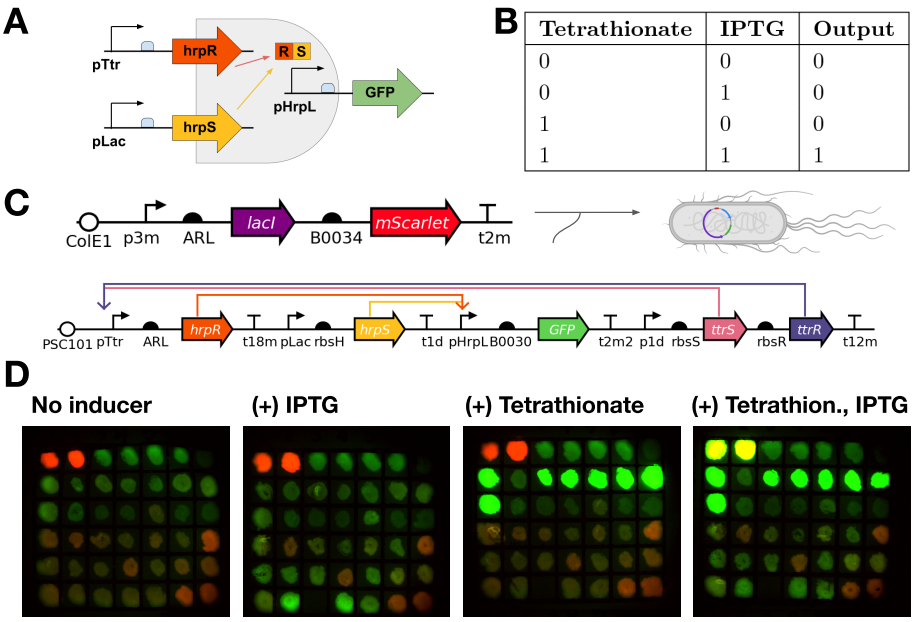

Tetrathionate	IPTG	Output
0	0	0
0	1	0
1	0	0
1	1	1

Figure 4: AND Gate Design and Screening. A. The σ54-dependent promoter hrpL is activated by two activators: hrpR and hrpS. The expression of hrpR is driven by pTtr, the tetrathionate response promoter. The second activator, hrpS, is driven by pLac which is induced by IPTG. Should the AND gate function properly, we expect GFP expression only when both inducers are present. **B.** A truth table displaying the expected output. **C.** The circuit diagram for co-transformed plasmids. The PSC101 backbone contains KanR, conferring kanamycin resistance. The ColE1 backbone contains ChlorR, conferring chloramphenicol resistance. **D.** Plate screening of AND gate constructs. LB plates contained max inductions of IPTG (1 mM), Tetrathionate (1 mM), neither, or both. Colonies were streaked on all four plates. Successful colonies were red fluorescent in all plates, signifying constitutive mScarlet production, and green fluorescent on the double inducer plate, signifying AND activation. Colonies in the top left two positions were miniprepped and re-transformed into Nissle.

screening and plate reader assays, we confirmed the selective AND gate functionality of one dual-plasmid construct, shown in Figure 5-A. In our experimental results, we observed a 6-fold induction once tetrathionate and IPTG are both added and minimal expression in the one or no inducer conditions. We further show the AND gate displays digital-like activation across a range of both inputs Figure 5-B. To the best of our knowledge, this is the first functioning inflammatory sensing AND gate in *E. coli* Nissle.

In applications of our system, we can imagine a scenario where our microbe experiences one of the inputs before the other. For example, if the AND gate senses epithelial proximity and tetrathionate, it is likely tetrathionate may be sensed first, since it is a small biomarker that may be diffuse some distance away from the site of inflammation. We wanted to test our circuits response time in either case: if IPTG or tetrathionate are present for five hours before

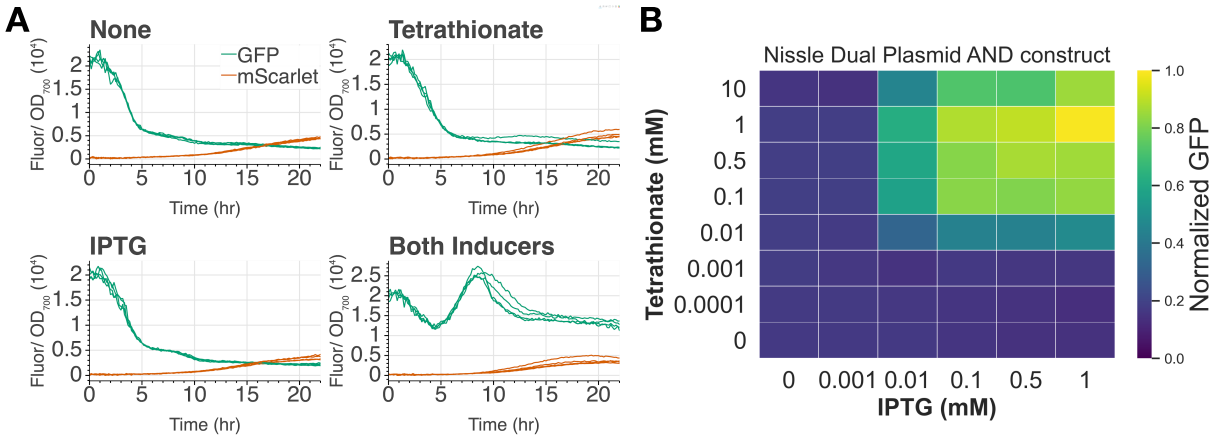

Figure 5: AND Gate Experimental Results. A. Plate reader assay for Nissle AND constructs. Maximum induction of 1 mM tetrathionate and 1 mM IPTG was used. Fluorescence values were normalized to OD700 readings. At the experiment's onset, low OD causes high normalized values. Maximum induction is achieved by hour 8. **B.** Heatmap of increasing inducer concentrations. Values displayed are GFP fluorescence normalized to OD, divided by the maximal value, which was achieved at 1 mM IPTG and 1 mM tetrathionate. To test the upper bound of tetrathionate sensing, 10 mM was used, showing slight decrease from the 1 mM condition. This could be caused by resource loading or cell toxicity at this concentration.

the other inducer appears. To do this, we performed the inducer grid plate assay shown in Figure 6. We discovered that cells grown in IPTG and then spiked with tetrathionate reached their maximal induction level faster than those grown in tetrathionate and then spiked with IPTG. Note the height of the peak may not be informative, due to differences in Biotek fluorescence levels. However, it does seem to be the case that tetrathionate activation has faster dynamics than the pLac promoter. Further investigation into these time scales may allow estimates of activation regimes once this circuit is inside gut conditions.

2.4 Design Space Exploration with an AND Gate Model

Like the two-component system model, we modeled the AND gate circuit by describing all of the different mechanisms and components discussed in the previous section. With this model, we explore two key design aspects of the system — the effect of RNA polymerase binding selectively with the combinatorial promoter in the presence of both activator proteins and the effect of initial conditions of the LacI repressors. This design space exploration points towards further design optimizations possible in the circuit, which would be essential to harness when implementing this AND gate in the gut microbiome.

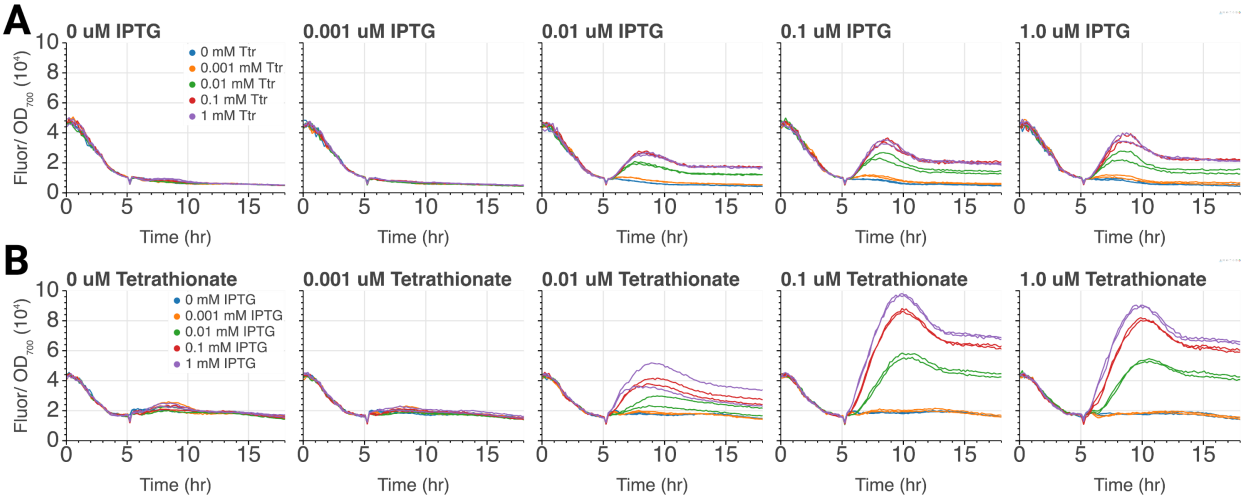

Figure 6: AND Inducer Spike Experiments. A. LM42 is grown in varying amounts of IPTG until the five hour mark, when five concentrations of tetrathionate are added to the wells. **B.** Cells are grown in tetrathionate until hour five, when varying amounts of IPTG are added.

Effects of RNAP Binding

As shown in Figures 7-A and 7-B, RNA polymerase can bind to the combinatorial promoter, pHrpL, either when both the activators hrpR and hrpS are present, or when only one of those is bound to the promoter. Of course, this binding specificity is not experimentally tunable and depends on the designed constructs and chassis. To study all of these possible interactions and their effects, we model the corresponding reactions in a coarse-grained model. We model the logic gate circuit with a non-zero amount of both split activator proteins, hrpR and hrpS (R and S, respectively). Using this logic gate model, we performed preliminary parameter searches to study the combinatorial promoter dynamics.

Due to their high sequence similarity, it may be possible for a single hrp activator (R or S) to gain the ability to activate transcription, perhaps through mutations in binding domains. To account for this case, we allow a single activator-DNA-RNA polymerase complex to activate transcription at a decreased rate relative to the two activator complex. In Figure 7-C, we simulate this effect by varying the unbinding rate of RNAP to the pHrpL:hrpR complex by more than 100-fold. We begin with a very low unbinding rate, signifying that RNAP is able to transcribe the single activator complex, pHrpL:hrpR, more readily. Indeed, we see that even small amounts of hrpR are now sufficient to activate the AND gate. The circuit still activates readily at high hrpS, since the $k_u^{hrpR:hrpS} < k_u^{hrpR}$, conferring a preference for the double activator case. Increasing the k_u^{hrpR} 100-fold in Figure 7-C results in AND gate functionality. This implies that the AND gate's functionality depends on the RNA polymerase's binding specificity to the combinatorial promoter when both activating signals are present. The experimental result for this AND gate implemented in Nissle, as shown in Figure 5, displays similar performance as in the model simulations in the last panel of Figure 7-C. Hence, we can hypothesize about this unknown mechanism of RNAP binding and conclude that it is indeed a specific binding that occurs primarily when both activators

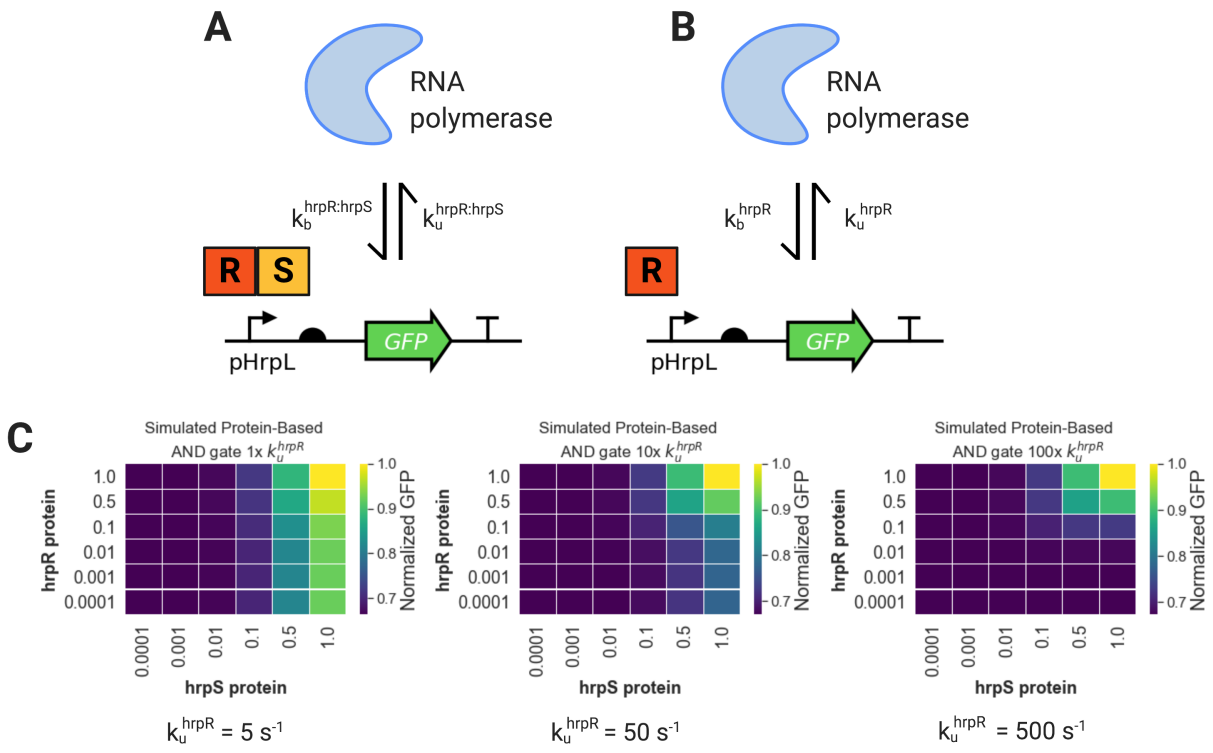

Figure 7: Parameter Tuning in Protein AND Gate Model. A. Both regulators may bind to the promoter region, creating a complex capable of being transcribed. RNA polymerase binds and unbinds with the rates shown. **B.** A single activator is also able to trigger transcription. Here, we show the effects of tuning hrpR's ability to trigger transcription. **C.** Examples of how decreasing off-rate of RNAP to the pHrpL:hrpR affects the output. We see significant loss of reliance on the second activator, hrpS, when hrpR is allowed to form an active transcription complex that unbinds less frequently. Note, this result is symmetric. If we model hrpS, the AND gate functionality changes in ways consistent to those shown here.

are present.

To further analyze the system behavior we expanded the coarse-grained model of the AND gate to include the expression of the two activators, hrpR and hrpS as well. We established earlier that the promoter can initiate transcription when both activators are bound, but also at a slower rate if one or neither activator binds. The detailed model consisting of all the transcription and translation reactions of this construct also confirms this. In addition, using the detailed model, we can simulate and understand the dynamics of the activator transcript and protein levels as well as the dynamics of the reporter transcript and its expression level. We developed this detailed model using BioCRNpyler [45] and for all model simulations, we used parameters and initial conditions consistent with those found

in the *E. coli* literature [50].

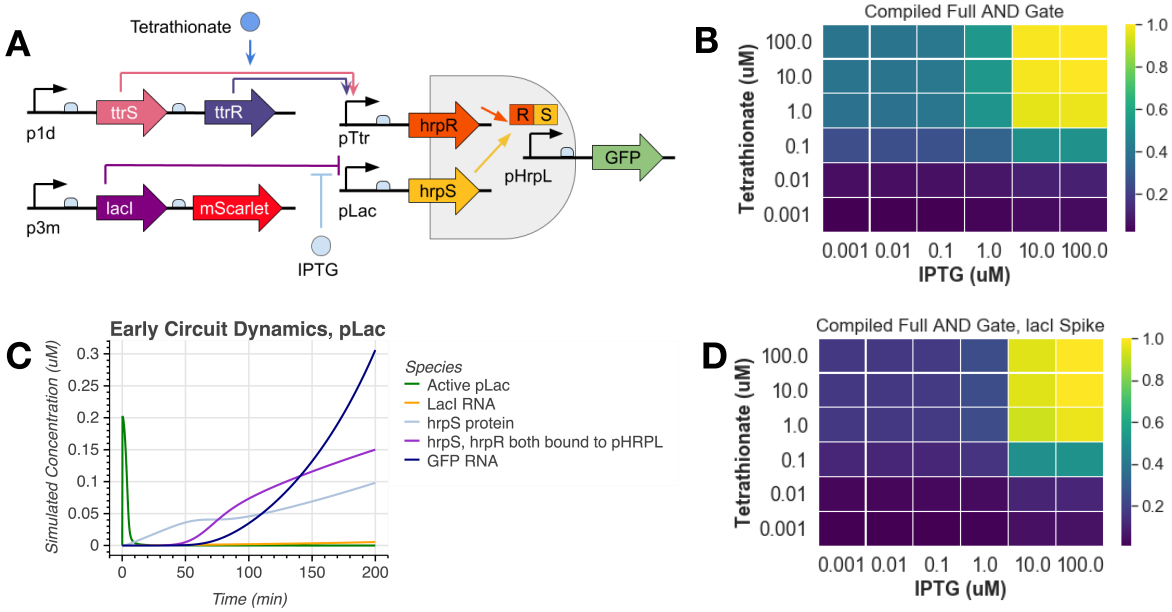

Figure 8: Full AND Gate Model. A. We model expression of the two split activator components. This detailed model allows us to tune various parameters to better understand dynamics. **B.** In the simulated heatmap, we see leak along the IPTG axis, telling us there is some underlying activation of pLac even when IPTG concentrations are below the activation threshold. **C.** When we input 0 mM IPTG and 1 mM tetrathionate, we see that there is still a burst of active pLac in the beginning of the time course. This burst of hrpS expression led to increasing amounts of GFP throughout the simulation. **D.** This led us to spike in 1 mM lacI at the beginning of the experiment, preventing the initial spike of unrepressed pLac.

Effects of Repressor Initial Conditions

To study the effect of initial conditions for the LacI repressor, we use the LacI repression mechanism that we modeled in our full system description. Two LacI molecules bind to DNA forming a repressed complex that can not be transcribed. A single IPTG molecule can sequester LacI in solution, preventing the repressor complex from binding to DNA. IPTG can also bind to the LacI complex bound to DNA, releasing LacI from the operator region. The AND gate activator hrpR is under the expression of the pLac promoter. The circuit schematic corresponding to the model is shown in Figure 8-A. Note that when LacI is not bound to pLac, hrpR is expressed constitutively. We explore the model simulations by plotting the steady state GFP values under different input conditions as shown in the heatmaps in Figure 8-BD.

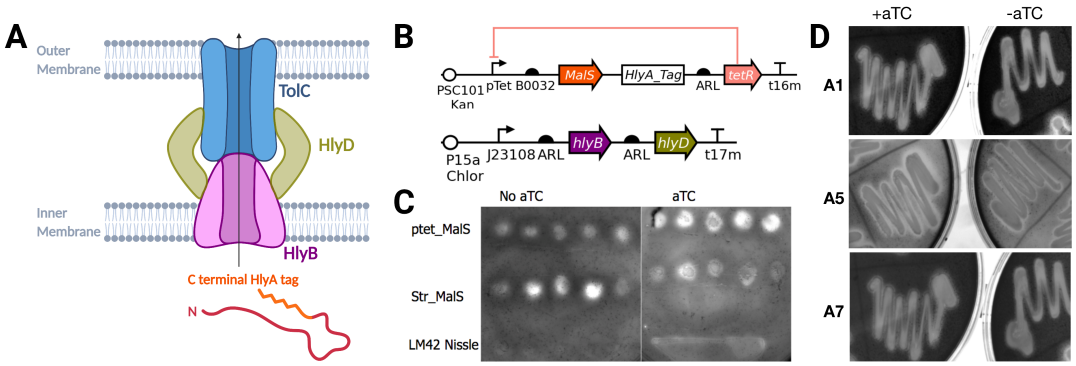

Figure 9: HlyBD Secretion System Engineering. A. The three components of the secretion system, shown with a C-terminal HlyA tagged protein. **B.** The two plasmid secretion system used for testing. MalS encodes a starch degrading enzyme. The 64 amino acid HlyA tag was used. **C.** Iodine-stained starch plates with 10 tested colonies. The first row contains aTC inducible MalS, whereas the second is a strong constitutively expressed MalS. The bottom row is a negative control Nissle cell without secretion machinery or MalS. The addition of aTC appears to activate Tet inducible MalS construct, which has less starch present than in the no inducer condition. **D.** Three more constructs tested with the iodine starch plate assay, where aTC appears to increase starch clearance.

A key design aspect that results from this analysis is that if we start with no LacI present, we obtain leaky activation of the AND gate independent of the IPTG levels as shown in Figure 8-B. This is counterintuitive since LacI is constitutively expressed in the system. A possible hypothesis could be that the delay in transcription of LacI leaves enough time for hrpR expression, even at low levels, hence giving a leaky reporter expression. By looking at the time-course dynamics of the system carefully, we find that this is indeed the case. We observe that there is a sharp spike in actively transcribing pLac. This causes small amounts of hrpR transcription, which is enough to activate the AND gate. It is important to note that increasing the rate of LacI transcription/translation and decreasing the rate of pLac transcription does not fix this issue. However, we know that the engineered microbe is such that it will always have cellular LacI diluted in from its parent. So, the case study with zero initial condition for LacI is not applicable in practice. To account for this in our model, we simply spiked low concentrations of LacI as an initial condition, thus resulting in recapitulation of the expected AND gate dynamics as shown in Figure 8-D.

2.5 Secretion System Optimization

To increase yield of any eventual therapeutic output, the type I secretion system (T1SS) was investigated. A well-characterized T1SS was constructed. First, a plasmid containing HlyB and HlyD sequences was created and transformed into electrocompetent tet-inducible HlyA-tagged MalS Nissle cells. As shown in Figure 9-B, the tetR repressor was placed at the end of the inducible construct because Nissle does not contain genome-integrated repressors. A fluorescent version of this construct was first screened to identify proper

ribosome binding site strength. As the stoichiometry of HlyB and HlyD is important for secretion efficiency, the ARL was used preceeding these genes. This necessitates wide-scale screening to find optimal expression levels of these secretion machineries. As shown in Figure 9-C, the starch agar plate test was first used to identify potential success of this system. An increase in cleared (light) areas on the plate signify increased clearance of starch, and thus an increase in the extracellular amylase MalS. It is interesting to note that LM42, a Nissle strain without secretion machinery or MalS does not have high clearance of starch. However, the inducible construct does appear to have larger halo clearance upon MalS activation. While the repressor level of tetR was optimized with a fluorescence screen, it appears there is still leak in the no aTC condition. Because these qualitative results are hard to interpret, we developed a quantitative assay to read out starch concentration.

We created a Hamilton STARlet protocol to add 30 uL of iodine to 100 uL of varying amounts of starch media. Initial tests shown in Figure 10-B show that the positive control, PY79, only had slightly greater starch degradation than the engineered pTet-inducible MalS construct, A2, which has the HlyBD plasmid as well. Motivated by this result, we created inducible AND gates responsive to tetrathionate and aTC. Notably, these cells do not have the HlyBD secretion system. Some constructs see a decrease in starch in the activated case, suggesting there is either large amounts of leak out of the membrane, or that this assay is flawed. Considering the AND gate GFP constructs also had decreases in starch compared to media only, it is likely the cell density is interfering with the reading and convoluting the result.

2.6 Successful Secretion in *E. coli* Nissle and HB2151

Due to the variability in our developed starch assay, a new approach for assaying secretion was explored. In particular, protein gels to measure extracellular presence of the secreted protein were explored. To optimize the protein gel protocol, we obtained previously characterized secretion plasmids [35], shown in Figure11-A. The first plasmid expresses the secetion machinery proteins hlyB and hlyD and was first characterized in [51]. In our earlier tests, we obtained our sequences for these genes from the iGEM Registry. While the protein translation sequences are identical, the previously characterized secretion plasmid from [35] also contains a short segment of hlyA that precedes hlyB. It is unclear if this segment is necessary for secretion, and further testing is needed to ascertain this. The second plasmid encodes an inducible VHH antibody against α-amylase. This sequence is succeeded by a series of protein purification tags, and then the 651 bp hlyA export tag. In Figure11-C, we first confirmed that this secretion plasmid the previously characterized secretion system is functional. Using an SDS-PAGE gel, we see bands of the expected size in both co-transformed *E. coli* Nissle and HB2151, which is the strain used in [35]. To the best of our knowledge, this is the first successful nanobody secretion through the hemolysin pathway in *E. coli* Nissle.

2.7 Replacing Backbone and Promoter Maintains Secretion Efficacy

We sought to replace the inducible VHH against α-amylase with anti-inflammatory AND gate constructs, which we previously optimized on the PSC101 backbone. However, the secretion machinery constructs were expressed on the PSC101 backbone as well. Because

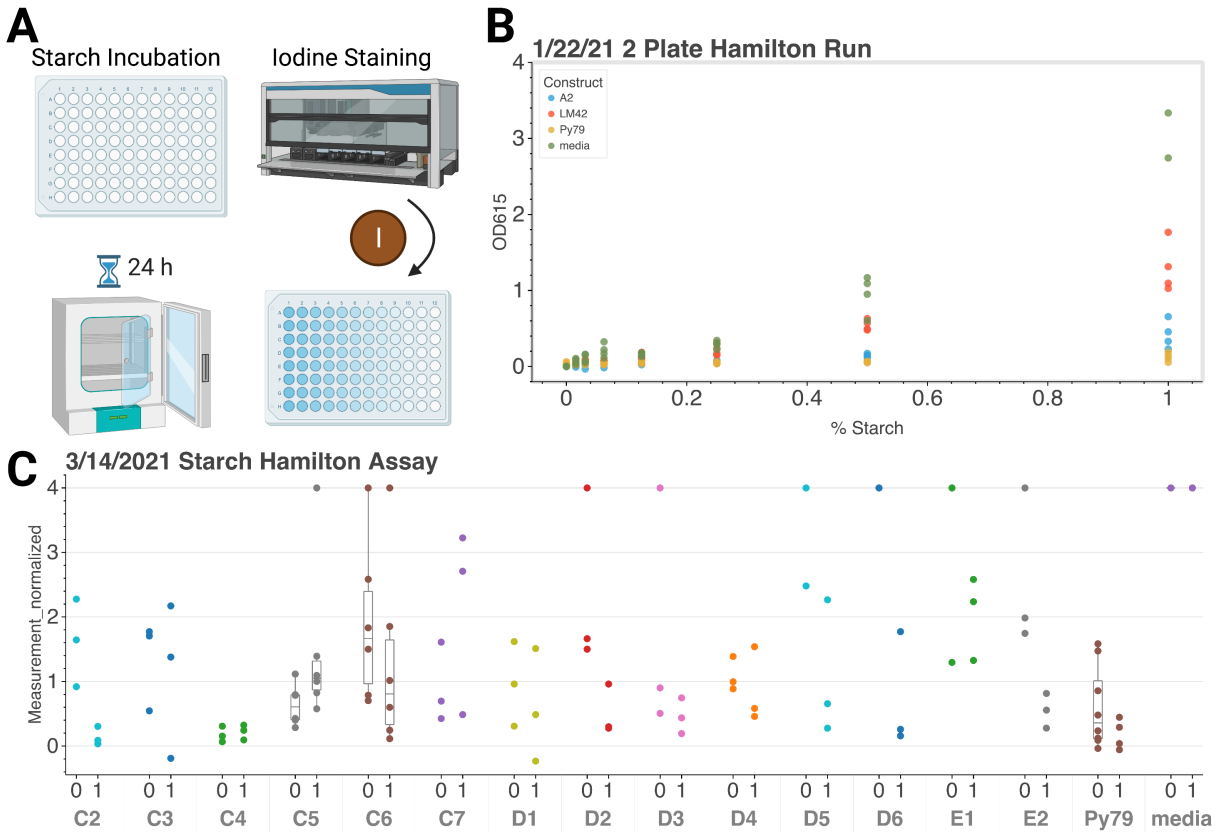

Figure 10: Secretion Liquid Culture Iodine Assay. A. A diagram depicting the workflow. Cells are grown in varying concentrations of starch LB media. After 24 hours, cultures are stained with 30 uL Gram's iodine. **B.** Initial screens show that media has highest absorbance. Nissle cells without secretion or amylase (LM42) has next highest starch concentrations. Engineered pTet inducible MalS shows almost same starch concentration as Py79, a *B. subtilis* strain that constitutively secretes amylase. **C.** AND gate inducible constructs with att site and malS with hlyA tag (C2-C4), malS with hlyA tag (C5), malS (C6-D4), and att site with GFP (D5-E2). While malS strains appear to consume starch in presence of inducers (shown as 0 or 1 on the x-axis), their measurements are still about the same concentration as a non-starch degrading strain that only contains GFP.

the AND gate constructs required several rounds of optimization to maintain the proper expression of regulatory components to minimize leak, we decided to approach engineering the secretion components onto a different plasmid instead. During the Gibson assemblies, we also created a construct that expressed hlyB and hlyD under the constitutive J23100 promoter rather than pLac. This would help us determine if constitutive secretion machinery expression over-burdens the cell, as most previous engineering applications had used inducible secretion control instead. This choice was also made to disentangle the expression of the secretion machinery plasmid and the protein expression plasmid, which were, until

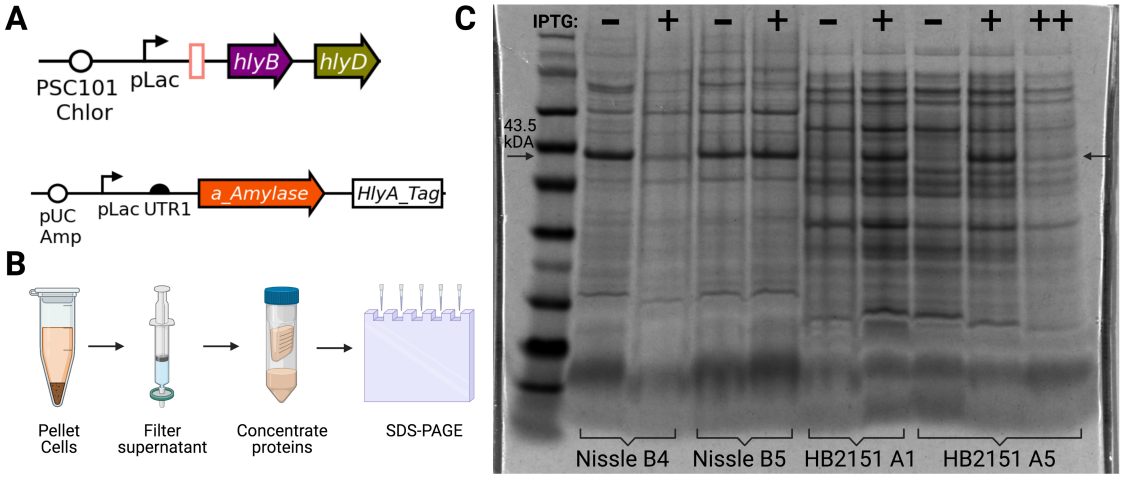

Figure 11: Protein Gel to Assay Secretion. A. Two plasmid components of functional secretor cells. First, the secretion components are expressed by pVDL9.3, on the pSC101 Chlor backbone. Note the pink box that precedes hlyB is a short 90 bp segment of hlyA. The nanobody to be secreted, anti α-amylase, is under pLac expression on the pUC Amp backbone. Both plasmids were transformed into either *E. coli* Nissle or *E. coli* HB2151. Note that Nissle does not have lacI on the genome, while HB2151 does. Thus, Nissle should be secreting even without IPTG. **B.** Schematic of the workflow. Cells were grown overnight and pelleted as described in the Methods. The supernatant was then filtered, which is critical to remove any bacterial cells still present, as this would interfere with conclusions about secretion. The supernatant is then concentrated and run on an SDS-PAGE gel. **C.** Two colonies of either Nissle or HB2151 containing the plasmids were tested, with (+) and without (-) IPTG. ++ signifies 10x IPTG to determine if overexpressing the secretion machinery and protein would reduce yield. Results show that the hlyA-tagged nanobody, which is 43.5 kDa, is present in the supernatant in all conditions, suggesting some leak in the pLac promoter for HB2151.

now, both under control of pLac. We co-transformed the new backbone secretion plasmids with the plasmid containing VHH against α-amylase tagged with hlyA. The new backbone, p15A, maintains active secretion with the pEHLY plasmid in Figure 12-C, as shown by the correct size band present in IPTG positive samples. As before, we see some interesting smaller fragments. Interestingly, it has been noted that shorter hlyA fragments may be sufficient to confer secretion through the hemolysin transporter. It is possible these bands correspond to early translation termination, causing a shorter hlyA tag while maintaining effective secretion. Further investigation into the identity of these fragments is needed. For the next stage of our engineering pursuit, colonies A5 and B1 were chosen as successful secretion constructs.

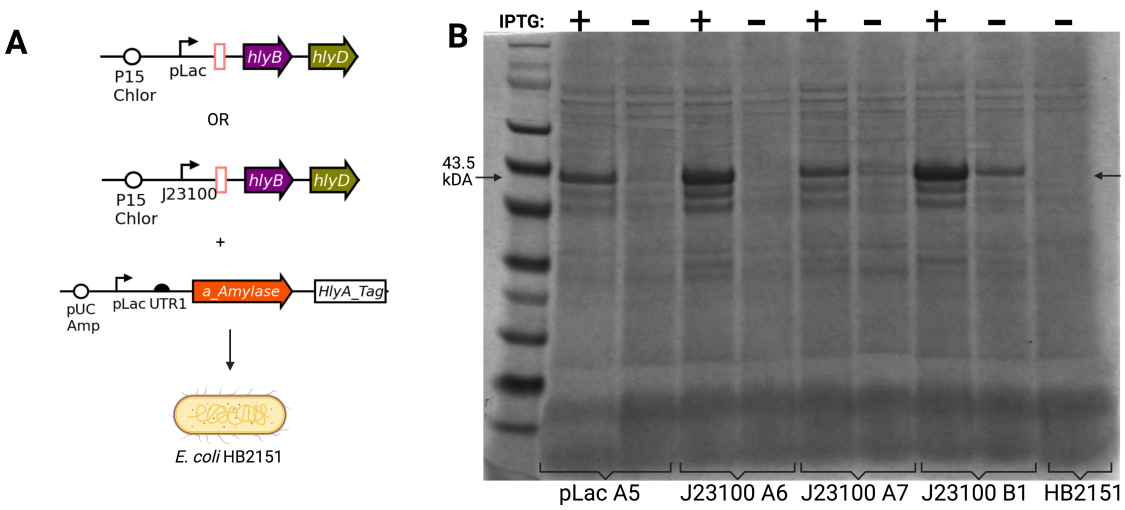

Figure 12: Replacing Backbone Maintains Secretion. A. The secretion components were Gibson assembled from pVDL9.3 onto p15A Chlor backbone. During the assembly, the pLac promoter was replaced in some constructs. Secretion machinery plasmids were co-transformed with pEHLY into HB2151. Note that the nanobody on pEHLY is driven by pLac, so no secretion is expected in the absence of IPTG. **B.** An SDS-PAGE gel stained with Coomassie brilliant blue. Both the pLac and J23100-driven expression of VHH against α-amylase show strong bands where expected. The right-most lane contains HB2151 without either plasmid. Interestingly, B1 shows a strong band even without the presence of IPTG. This suggests leak, where α-amylase is expressed in the absence of IPTG.

2.8 Secreting Anti-Inflammatory Molecules

Once confirming our new hlyBD expression plasmid was functional when paired with the previously tested VHH against α-amylase construct, we tested whether IL-10 and IL-22 could be secreted. First, constructs containing pLac-inducible human IL-10 or mouse IL-22 were assembled onto the ColE1 high copy number backbone. These plasmids were sequenced verified and co-transformed into *E. coli* HB2151 with the constitutive hlyBD plasmid, as shown in Figure 13-A. The VHH against α-amylase was used as a positive control. While the inducible IL-10 construct failed to show a band of the expected size, inducible IL-22 had a very faint band present in the supernatant. To the best of our knowledge, this is the first successful secretion of mouse IL-22 with the hemolysin secretion pathway.

Upon further inspection of the secretion constructs, it was discovered that there were stop codons present before the HlyA tag in both IL-10 and IL-22. This is likely the cause for low secretion output in IL-22, and may be the reason there is no external IL-10 seen here. We can analyze the bands inside the cell, denoted with "pellet" above the blot shown in Figure 13-B. In the IL-10 condition, there are three bands that are consistent with intracellular IL-10 production. First, the IL-10 monomer without the HlyA tag has a weight of 19 kDa. The dimer is 38 kDa, and the trimer is 57 kDa. It seems that all three of these bands are present internally in the IL-10 samples, leading us to believe the inducible IL-10 construct is successfully producing monomeric, dimeric, and trimeric forms of IL-10. The HlyA-tagged

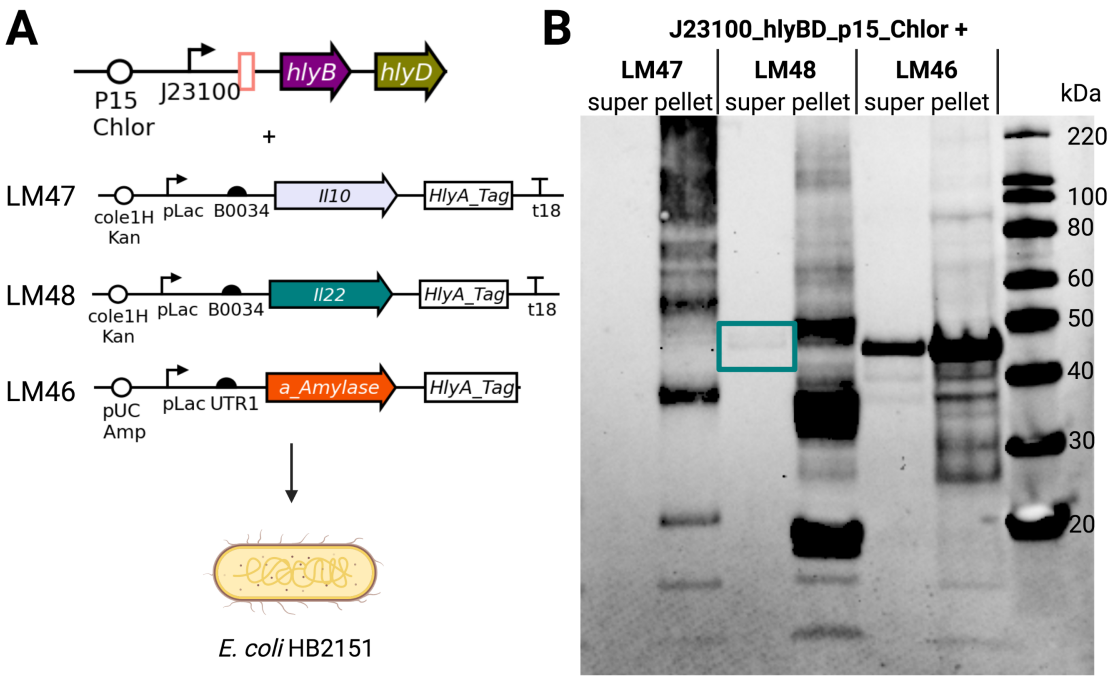

Figure 13: Low Yield Anti-Inflammatory Secretion. A. The successful constitutive secretion machinery construct from Figure 12-A was isolated and co-transformed with inducible IL-10 or IL-22. The positive control is colony B1 from Figure 12-B, labeled here as LM46. **B.** A western blot with anti-His antibodies, which bind to N-terminal His tags present on all protein secretion constructs. The expected bands for HlyA-tagged monomers of IL-10, IL-22, and VHH against α-amylase are 48 kDa, 46 kDa, and 43.5 kDa, respectively. There are bands of the correct size in the supernatant of both the IL-22 and positive secretion control.

IL-10 monomer is expected at 48 kDa. It is unclear from this blot whether a band of that size is present. This is likely caused by the stop codon mentioned above.

In IL-22, the expected intracellular band sizes are 17 kDa, 34 kDa, and 51 kDa for the monomer, dimer, and trimer respectively. These three bands can be seen in the IL-22 construct's pellet, signifying that these three products are present inside the cell. Slightly below the IL-22 trimer, we see the small intracellular band for HlyA tagged IL-22 monomer, present at 46 kDa. This is the same size as the secreted band present in the supernatant, supporting the the conclusion that secretion of the HlyA tagged IL-22 monomer was successful.

From here, Gibson assembly was used to remove the stop codon from the IL-10 and IL-22 constructs, towards the goal of improving yield in IL-22 and observing secretion in the IL-10 construct. To further increase the amount of secreted anti-inflammatory product, B0034 was replaced with UTR1 as the RBS preceding both IL-10 and IL-22. This choice was also made because the anti-inflammatory constructs would next be incorporated into the AND gate plasmid, which is on a lower copy number plasmid, PSC101, compared to ColE1. Sequence verified plasmids were co-transformed into *E. coli* HB2151 with either the inducible hlyBD plasmid, LM61, or the constitutive hlyBD plasmid, LM62. Constructs are

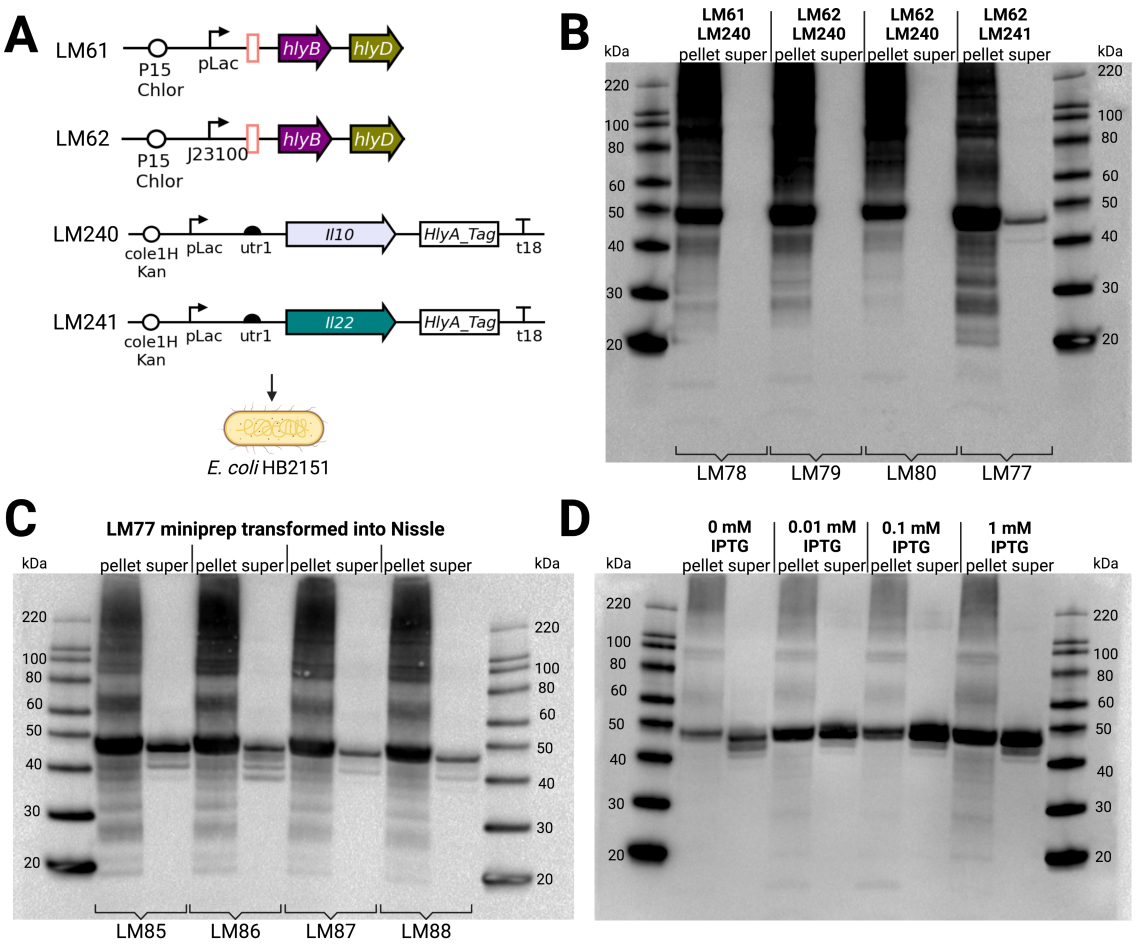

Figure 14: High Yield IL-22 Secretion in *E. coli* HB2151 and Nissle. **A.** Successful secretion machinery constructs LM61 and LM62 were isolated from colonies A5 and B1, respectively, in Figure 12-B. Stop codons were removed from IL-10 and IL-10 constructs and re-assembled into the ColE1 high copy backbone. **B.** A western blot with anti-His antibodies showing a strong band signifying IL-22 secretion. IL-10 constructs have strong intracellular bands, but fail to produce bands in the supernatant. **C.** A western blot with anti-His antibodies showing success of transferring LM77's secretion plasmids into *E. coli* Nissle. All colonies display expected bands inside and outside of the cell. **D.** A western blot with anti-His antibodies showing an IPTG induction experiment with LM77.

shown in Figure 14-A. Colony PCR was then performed to confirm that both the secretion machinery and the anti-inflammatory expression plasmid were present in the cell. Four successful colonies were then assayed for IL-10 or IL-22 secretion.

While all colonies display strong bands inside the cell, it appears that only the IL-22 colony, LM77, is able to secrete the product of interest, shown in the blot in Figure 14-B. There is also a faint band below the product of interest, at around 40 kDa. It is unclear what this fragment is, and further investigation is needed to determine this. While IL-10

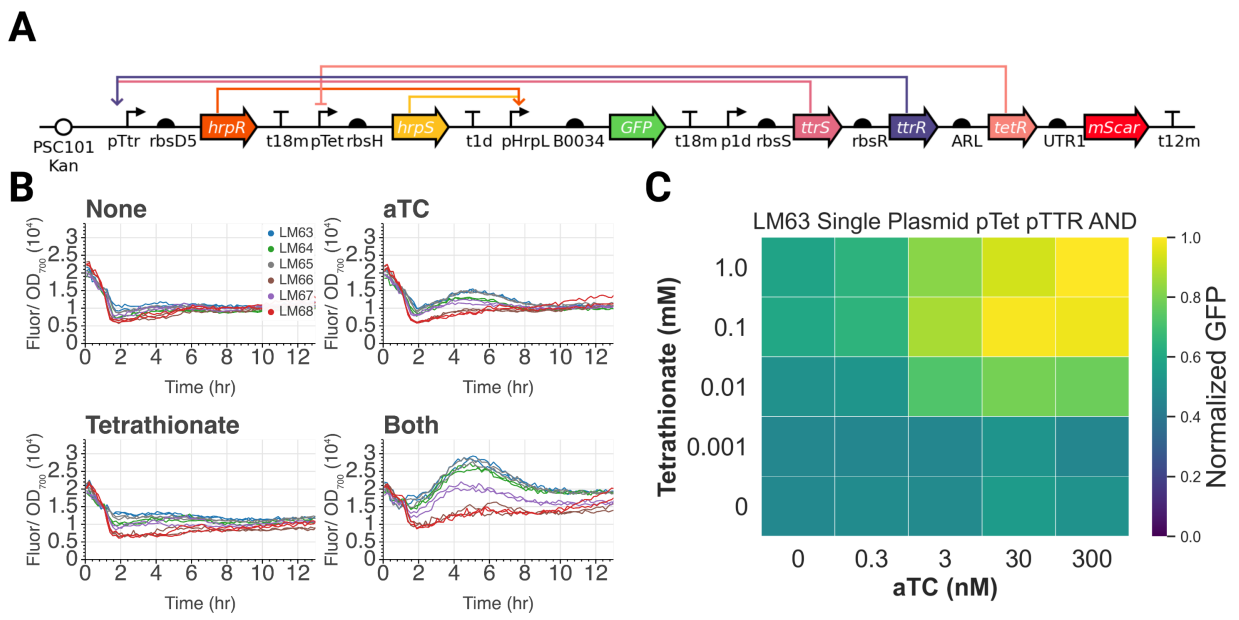

Figure 15: Single Plasmid AND Gate. A. The plasmid map for the single plasmid pTet and pTTR inducible AND gate. The RBS preceding tetR is an ARL such that plate screening could be used to identify correct inducer activation. **B.** A plate reader assay showing OD-normalized GFP readings for six AND colonies. Final aTC concentration is 300 nM and final tetrathionate concentration is 1 mM. The highest induction colony, LM63, was chosen for future analyses. **C.** Induction grid for LM63. Peak induction is achieved when both inducers are present.

colonies express large amounts of HlyA tagged IL-10 monomer inside the cell (present at 48 kDa), there does not appear to be a visible band outside of the cell. It should be noted that this blot was later over-exposed for one minute, and a faint band appeared in LM78's supernatant lane. Regardless, it is unclear why IL-10 fails to be secreted. It is known that the hemolysin secretion pathway secretes proteins in their unfolded state, starting with the C-terminal end. The size of IL-10 tagged with HlyA is approximately 48 kDa, which is within the range of products that the hlyB-hlyD-tolC secretion pathway has secreted before. We showed here IL-22, a product of size 46 kDa, could also be secreted. The hemolysin secretion system's native product is HlyA, which is 107 kDa. It has been shown that the size of the product does not play a role in the rate of secretion [33], but it is known that the rate of folding plays a role in whether the secretion mechanism stalls during extruding the product. It may be the case that mouse IL-10 folds too quickly, causing it to either stall in the secretion pathway or fail to enter altogether.

The plasmids in LM77 were then isolated through miniprep and transformed into electrocompetent *E. coli* Nissle cells. Nissle does not have the lacI repressor on the genome, and thus does not need IPTG induction in order to express the pLac-inducible IL-22 construct. bands were seen in all colonies, signifying that Nissle can secrete IL-22 through the hemolysin secretion pathway. Interestingly, there appears to be more fragments ranging from 40 kDa up to the correct band size at 46 kDa. These fragments were also seen in an IPTG induction

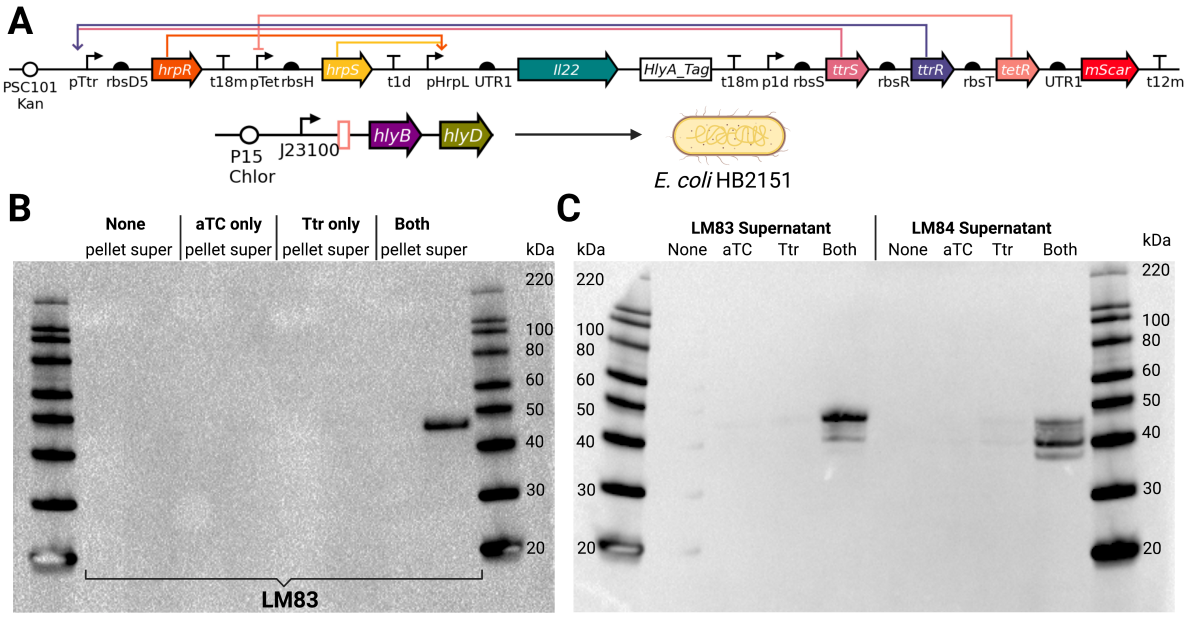

Figure 16: AND Gate IL-22 Secretion. A. LM63's backbone was amplified and the AND product, driven by pHrpL, was changed from GFP to HlyA tagged IL-22. Constructs were co-transformed with constitutive expression hlyBD into *E. coli* HB2151 and sequence verified. **B.** A western blot with anti-His antibodies showing IL-22 secretion only when aTC and tetrathionate are present. **C.** A western blot with anti-His antibodies to verify results in **B**. LM83 has the correct band size at 46 kDa, with a smaller fragment present around 40 kDa. LM84 predominantly has the shorter fragment, signifying different folding or secretion rates.

experiment with LM77, the IL-22 secreting colony in *E. coli* HB2151. Here, we see that the band size does increase as the amount of IPTG increases. However, we also see IL-22 secretion in the 0 mM IPTG condition. This could represent leak in the pLac promoter, especially given the high copy number and strength of RBS that precedes the IL-22 sequence. With secretion of IL-22 verified in the single promoter induction case, we proceeded to test secretion in the AND gate.

2.9 AND Secretion of IL-22

Recall the two plasmid AND gate optimized in Figure 5 was built with lacI and mScarlet on a separate plasmid. As we added secretion machinery components, we wanted to reduce the final plasmid load on our cells and thus chose to consolidate the AND gate into a single plasmid. Overall, the single plasmid AND gate is leakier than the two plasmid system, likely because the repressor is now on a lower copy number plasmid than it was previously. The final construct is shown in Figure 15-A. While we performed one round of ARL screening for the RBS preceding the repressor, further optimization may be needed to reduce leak in the system. We show the time course results of the single plasmid AND construct in Figure 15-B.

Interestingly we see maximal induction at around 5 hours, which is faster than the 9 hour peak we saw in the two plasmid AND gate shown in Figure 5-A. As before, we tested the circuit with an inducer grid and saw maximal induction when both inducers were present, although the dynamic range is lower than that of the two plasmid construct.

We amplified the backbone of the LM63 construct and replaced the AND gate promoter GFP part with the AND gate promoter IL-22 construct. This would allow for secretion of IL-22 only when the AND promoter is activated, in the presence of both inducers. Note that because the successful IL-22 secretion construct was on the ColE1 backbone, the copy number on the AND PSC101 plasmid would be lower. We thus decided to keep UTR1 as the RBS preceding IL-22, to allay concerns that the signal would be too weak to detect. The final construct is shown in Figure 16-A. We co-transformed with the constitutive secretion machinery plasmid, since this was successful in the previous IL-22 secretion experiments. Further testing is needed to confirm that the pLac inducible hlyBD plasmid is successful here as well.

Two colonies were found to have full-length, sequence verified AND gates. We tested the first colony, LM83, to determine whether the AND secretion construct was active only in the presence of both inducers, shown in Figure 16-B. We see the correct size band for the IL-22 monomer tagged with HlyA in the supernatant when both inducers are present. Interestingly, there does not appear to be a band in the pellet of the both inducer condition. This potentially signifies that the rate of production and secretion are balanced now that the construct is on PSC101 as opposed to the higher copy ColE1. The supernatant from this experiment was saved and re-run alongside the second colony, LM84, shown in Figure 16-C. After exposing for a longer period of time, we do see a potential faint band in the tetrathionate only condition for both LM83 and LM84. It also appears that LM84's predominant secretion product is smaller, around 40 kDa. Further investigation is needed to ascertain the identity of this product, and to understand why the same construct in two different cells may have different secretion rates.

3 Methods

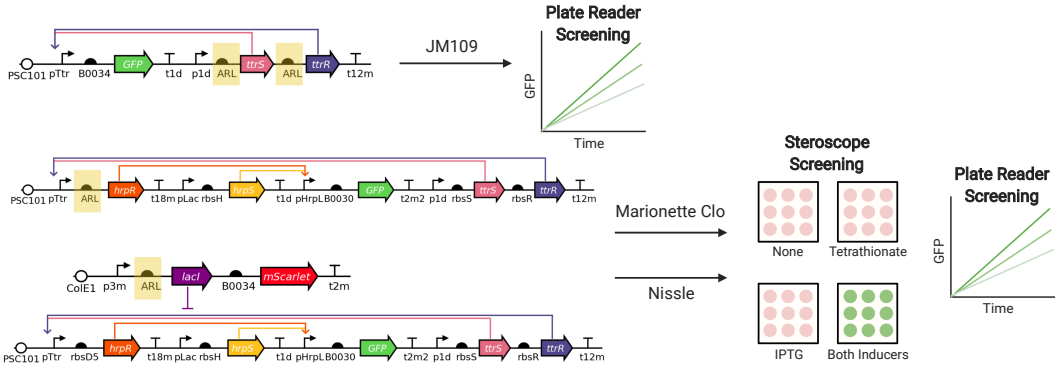

Figure 17: Constructs and Screening Stages. The tetrathionate construct was optimized using plate reader screening, while the AND gates were first screened on inducer plates. Stereoscope images were taken, and colonies that were OFF in all cases except both inducers were then chosen for further plate reader assays. Note in the full AND gate, mScarlet is constitutively expressed, such that the one or no inducer plates are still red fluorescent.

3.1 Plasmid Construction

Plasmid maps and screening methods are shown in Figure 17. Sequences are available as GenBank files on Github [40]. Circuit diagram plots were created with DNAplotlib [52]. All constructs were assembled using 3G assembly, as described [47]. Constructs were sequence verified by sequencing (Laragen) after amplification with UNS primers. The sequence for ttrS was identified from Addgene PKD227. We obtained sequences for ttrR, and pTTR sequences from Addgene plasmids pKD233.7-3. gBlocks with these sequences were ordered from Twist Biosciences and resuspended in IDTE buffer. Logic gate parts were gifts from Martin Buck & Baojun Wang. hrpS was amplified from pBW213 (Addgene 61435) hrpR was amplified from pBW115 (Addgene 61434), pHrpL was amplified from pBW412hrpL-cIgfp (Addgene 61438). The BSAI cut site was removed from hrpS by Gibson assembly. B0030 and RBSH sequences were obtained from [25] and synthesized by IDT. Secretion plasmids pVDL9.3 and pEHLY were gifts from Luis Angel Fernandez. HlyBD genes were amplified from pVDL9.3 and inserted into vectors compatible with AND gate plasmids. The sequence for IL-10 was obtained from [53]. The sequence for IL-22 was obtained from [54] and codon optimized for *E. coli*. IL-10 and IL-22 sequences were ordered as gBlocks from IDT and resuspended in IDTE buffer.

3.2 Bacterial Strains

Tetrathionate regulator optimization circuits were transformed into chemically competent *E. coli* JM109 (Zymo Research). Optimization of AND gate constructs was performed

by making constructs with ribosome binding site library (5'-GAAAGANNNGANNNACTA-3') in front of regulators in chemically competent Marionette Clo cells prepared from Addgene [49]. Plasmids were miniprepped and re-transformed into electrocompetent Nissle 1917 (Mutaflor). Secretion experiments were performed in *E. coli* HB2151, a gift from Luis Angel Fernandez. Antibiotic concentrations used in all growth was 34 µg/mL chloramphenicol, 100µg/ml carbenicillin and 50 µg/mL kanamycin.

3.3 *In vitro* Aerobic Experiments

Colonies were screened using stereoscope images of LB agar inducer plates with 1 mM potassium tetrathionate (Sigma Aldrich), 1 mM Isopropyl-beta-D-thiogalactoside (Sigma Aldrich), or both. Successful colonies that were only fluorescent in the presence of both inducers were then used for *in vitro* screening.

These colonies were grown overnight in M9CA media (Teknova) to saturation. Cultures were then diluted 1:5 and grown for three hours. Characterization was performed in 96 well Matriplates (Dot Scientific, MGB096-1-1-LG-L). Where applicable, inducer media was prepared in M9CA and used to dilute outgrown cells. Plates were incubated at 37°C for 23 hours in a Biotek Synergy H2 plate reader with continuous shaking at 282 cpm. Optical densities (OD700) and fluorescence measurements were taken every 5 minutes from the bottom of the plate. GFP excitation and emission wavelengths were 483 nm and 510 nm, respectively. mScarlet excitation and emission wavelengths were 565 nm and 595 nm, respectively. Gain 100 was used for both fluorescence channels.

3.4 SDS-PAGE

To determine presence of secreted proteins, SDS-PAGE (polyacrylamide gel electrophoresis) was used. 1.5 mL of culture in appropriate inducers was grown overnight at 37°C. Cultures were then spun at 8,000 x g for 2 minutes to pellet cells. Supernatant was transferred to a 3 mL syringe, which was then passed through a 0.22 uM filter (Pall). Filtered supernatant was then concentrated using 30 kDa centrifugal filters (Amicon) according to supplier protocol. 5 ul LDS sample buffer (Thermo Fisher Scientific) was added to 15 uL of concentrated and incubated at 70°C for 10 minutes. 18 uL was loaded into NuPAGE Bis-Tris Gel (Thermo Fisher Scientific) with MES running buffer (Thermo Fisher Scientific) and run at 200 V for 20 minutes. The SeeBlue Plus2 pre-stained protein standard was used in lane 1 and lane 10 (Thermo Fisher Scientific). Gels were rinsed 3 times in DI water and then soaked for 1 hr in SimplyBlue SafeStain (Thermo Fisher Scientific) at room temperature with gentle rocking. Gels were destained in deionized water for 2 hours at room temperature with gentle shaking, and then imaged on Bio-Rad ChemiDoc MP.

3.5 Western Blotting

To verify identity of bands shown in SDS-PAGE gels, western blotting with anti-His antibodies was performed, except using the Magic Mark XP Western Protein Standard (Thermo Fisher Scientific) as the ladder. Samples were run on an SDS-PAGE gel as described above, but using the . Gels were then rinsed one time in deionized water and placed into a iBlot 2 mini transfer stack (Thermo Fisher Scientific). The transfer stack was loaded onto the

iBlot 2 Gel Transfer Device (Thermo Fisher Scientific) and run with the manufacturer's P0 protocol. After completion of the protocol, the membrane was soaked in Tris-buffered Saline (TBS) pH 7.6 for five minutes at room temperature with gentle shaking. The membrane was then soaked for 1 hour in blocking buffer (3% BSA in TBS). The membrane was then soaked for five minutes in TBS and run overnight on the iBind Western System (Thermo Fisher Scientific) according to manufacturers protocol. To detect His tags on secreted proteins, a Penta His HRP conjugate was used (Qiagen). A Goat anti-Rabbit IgG (H+L) Secondary Antibody conjugated to HRP (Thermo Fisher Scientific) was used to bind to the IgG-tagged ladder. After the binding protocol, the membrane was washed in TBS for five minutes at room temperature with gentle shaking. 20 mL of the SuperSignal West Pico PLUS Chemiluminescent Substrate was made up during the TBS wash. TBS was drained and the substrate solution poured over the membrane. The substrate was incubated for five minutes at room temperature with gentle shaking. The membrane was then imaged on Bio-Rad ChemiDoc MP using the Chemi Blot setting. Exposure times ranged from 2 seconds to 3 minutes depending on the strength of the band.

4 Discussion

This work demonstrates the engineering and modeling of a two-input AND gate for downstream therapeutic applications, where one input is the medically relevant inflammation signal tetrathionate. We optimized our circuit in *E. coli* Nissle, an attractive microbe for microbiome engineering projects due to its safety within the human and murine gut [55]. We modeled how our circuit would behave with different parameter values, informing our choices of engineered elements within the circuit. We varied ribosome binding sites experimentally, showing that the tetrathionate two-component system's stronger response could be recapitulated by varying ribosome binding rates in our model.

Computationally, we designed chemical reaction networks that model our microbial-based circuits *in silico*. We screened a wide variety of parameters, drawing from previously published datasets. In our sensing system modeling, we found that varying ribosome binding rates to regulator transcripts varies the tetrathionate response. Experimentally, we optimized the sensitivity of the two-component tetrathionate inflammation system in *E. coli* Nissle. We screened a library containing various RBS strengths and quantified the circuit's sensitivity as a function of fluorescent readout. The engineered strain LM19 demonstrated the largest dynamic range across therapeutically relevant concentrations of tetrathionate. We found experimentally varying RBS strength results in different fold changes consistent with our model.

We incorporated sensor logic by placing inputs of the split activator AND gate under the regulation of the tetrathionate and IPTG response promoters. After experimental tuning to minimize leak, this construct is activated when both tetrathionate and IPTG are present. By creating a chemical reaction network model of our full AND gate, we were able to identify potential causes for leak in our system. Experimentally, these cases may offer interesting pathways for studying protein-based logic gates. As we engineer additional functionality to this circuit, we hope that our *in silico* RBS tuning and insight into leak will offer us more understanding of our *in vitro* results.

We demonstrated successful secretion of IL-22 through the hemolysin pathway for the first time in *E. coli* Nissle, which has downstream applications in anti-inflammatory treatment. We combined our optimized AND gate with IL-22 secretion to show tetrathionate and aTC dependent secretion of our target protein. Through linking these two aspects of our project, we created a logic gate that can sense inflammation and a secondary input, and respond by secreting an anti-inflammatory cytokine.

In summary, our results demonstrate the usefulness of modular synthetic biological parts and circuit components to design circuits in microbial chassis capable of logically combining two independent input signals, one of which is associated with medical applications. We find that logic gates previously described by Wang et al. can be optimized in *E. coli* Nissle, allowing for future directions in OR, NOT, NOR, and NAND integration. We showed that the hemolysin secretion system characterized by Fernandez et al. can be used to secrete IL-22 in *E. coli* Nissle, opening new medical applications in microbiome engineering.

In future work, we will characterize the biological activity of our AND gate IL-22 secretion output. We will explore our circuit's ability to sense and respond to medically-induced inflammation and input signal aTC *in vivo*. The engineered circuit's functional stability moving from a controlled, *in vitro* environment to the gut microbiome's competitive

environment presents a significant challenge from the competition and metabolic burden perspective. As a continuation, we aim to engineer the second input increase spatial targeting within the gut.

Engineered microbes can deliver effective therapeutics with exquisite spatial and temporal resolution in medically relevant inflammatory conditions. Synthetic biology may offer advantages over traditional chronic inflammation therapies by designing targeted drug delivery to tissues affected by disease and rather than risk off-target effects. The models, logic optimization, and cytokine secretion reported here are a preliminary step towards this long term goal.

5 Acknowledgements

I would like to thank my thesis advisor, Professor Richard Murray, for being supportive as my aims and interests evolved over the course of this project. I want to thank Dr. Leo Green for his support, mentorship, and unwavering belief in me. I want to thank Andrey Shur for being patient and flexible for his guidance in developing new assays and constructs. Additionally, I want to thank John Marken for insight and discussion throughout the ups and downs of my project. Thank you Reed McCardell and Mark Prator for being great lab cohort-mates during this remote year. I want to thank Zoila Jurado for guiding me on protein gel assays. Thank you to Ayush Pandey and William Poole for technical guidance with modeling and analysis. Thank you to all members of the Murray lab for being supportive and giving excellent feedback during group meetings. I want to thank Professor Luis Angel Fernandez for secretion machinery. Logic gate strains were provided by Martin Buck & Baojun Wang. Some figures were created with BioRender.com. Thank you to Professor Justin Bois for teaching and supporting me throughout my time at Caltech. Thank you to my fellow BioEs and my forever Bi1x lab partner, Ankita Roychoudhury for emotional support. Thank you to my parents, family, and friends for supporting me deeply.

6 References

1. Schulz, M. D. *et al.* High-fat-diet-mediated dysbiosis promotes intestinal carcinogenesis independently of obesity. en. *Nature* **514.** Number: 7523 Publisher: Nature Publishing Group, 508–512. ISSN: 1476-4687. https://www.nature.com/articles/nature13398 (2020) (Oct. 2014).
2. Sharon, G., Sampson, T. R., Geschwind, D. H. & Mazmanian, S. K. The Central Nervous System and the Gut Microbiome. *Cell* **167,** 915–932. ISSN: 0092-8674. https://www.ncbi.nlm.nih.gov/pmc/articles/PMC5127403/ (2020) (Nov. 2016).
3. Kau, A. L., Ahern, P. P., Griffin, N. W., Goodman, A. L. & Gordon, J. I. Human nutrition, the gut microbiome and the immune system. en. *Nature* **474.** Number: 7351 Publisher: Nature Publishing Group, 327–336. ISSN: 1476-4687. https://www.nature.com/articles/nature10213 (2020) (June 2011).
4. Saeidi, N. *et al.* Engineering microbes to sense and eradicate Pseudomonas aeruginosa, a human pathogen. *Molecular Systems Biology* **7.** Publisher: John Wiley & Sons, Ltd, 521. ISSN: 1744-4292. https://www.embopress.org/doi/full/10.1038/msb.2011.55 (2020) (Jan. 2011).
5. Gurbatri, C. R. *et al.* Engineered probiotics for local tumor delivery of checkpoint blockade nanobodies. en. *Science Translational Medicine* **12.** Publisher: American Association for the Advancement of Science Section: Research Article. ISSN: 1946-6234, 1946-6242. https://stm.sciencemag.org/content/12/530/eaax0876 (2020) (Feb. 2020).
6. Daeffler, K. N.-M. *et al.* Engineering bacterial thiosulfate and tetrathionate sensors for detecting gut inflammation. *Molecular Systems Biology* **13.** Publisher: John Wiley & Sons, Ltd, 923. ISSN: 1744-4292. https://www.embopress.org/doi/full/10.15252/msb.20167416 (2020) (Apr. 2017).
7. Zeng, M. Y., Inohara, N. & Nuñez, G. Mechanisms of inflammation-driven bacterial dysbiosis in the gut. eng. *Mucosal Immunology* **10,** 18–26. ISSN: 1935-3456 (2017).
8. Loftus, E. V. Clinical epidemiology of inflammatory bowel disease: incidence, prevalence, and environmental influences. English. *Gastroenterology* **126.** Publisher: Elsevier, 1504–1517. ISSN: 0016-5085, 1528-0012. https://www.gastrojournal.org/article/S0016-5085(04)00462-7/abstract (2020) (May 2004).
9. Sun, Y. *et al.* The gut microbiota heterogeneity and assembly changes associated with the IBD. en. *Scientific Reports* **9.** Number: 1 Publisher: Nature Publishing Group, 440. ISSN: 2045-2322. https://www.nature.com/articles/s41598-018-37143-z (2020) (Jan. 2019).
10. Hazel, K. & O'Connor, A. Emerging treatments for inflammatory bowel disease. *Therapeutic Advances in Chronic Disease* **11.** ISSN: 2040-6223. https://www.ncbi.nlm.nih.gov/pmc/articles/PMC7003169/ (2020) (Feb. 2020).
11. Chan, W., Chen, A., Tiao, D., Selinger, C. & Leong, R. Medication adherence in inflammatory bowel disease. eng. *Intestinal Research* **15,** 434–445. ISSN: 1598-9100 (Oct. 2017).

12. Zhou, Z. *et al.* Engineering probiotics as living diagnostics and therapeutics for improving human health. *Microbial Cell Factories* **19,** 56. ISSN: 1475-2859. https://doi.org/10.1186/s12934-020-01318-z (2020) (Mar. 2020).

13. Hanson, M. L. *et al.* Oral delivery of IL-27 recombinant bacteria attenuates immune colitis in mice. eng. *Gastroenterology* **146,** 210–221.e13. ISSN: 1528-0012 (Jan. 2014).

14. Vandenbroucke, K. *et al.* Orally administered L. lactis secreting an anti-TNF Nanobody demonstrate efficacy in chronic colitis. eng. *Mucosal Immunology* **3,** 49–56. ISSN: 1935-3456 (Jan. 2010).

15. Sellon, R. K. *et al.* Resident enteric bacteria are necessary for development of spontaneous colitis and immune system activation in interleukin-10-deficient mice. eng. *Infection and Immunity* **66,** 5224–5231. ISSN: 0019-9567 (Nov. 1998).

16. Saraiva, M. & O'Garra, A. The regulation of IL-10 production by immune cells. en. *Nature Reviews Immunology* **10.** Number: 3 Publisher: Nature Publishing Group, 170–181. ISSN: 1474-1741. https://www.nature.com/articles/nri2711 (2021) (Mar. 2010).

17. Steidler, L. *et al.* Treatment of murine colitis by Lactococcus lactis secreting interleukin-10. eng. *Science (New York, N.Y.)* **289,** 1352–1355. ISSN: 0036-8075 (Aug. 2000).

18. Mauras, A. *et al.* A New Bifidobacteria Expression SysTem (BEST) to Produce and Deliver Interleukin-10 in Bifidobacterium bifidum. *Frontiers in Microbiology* **9.** ISSN: 1664-302X. https://www.ncbi.nlm.nih.gov/pmc/articles/PMC6308194/ (2021) (Dec. 2018).

19. Wei, H.-X., Wang, B. & Li, B. IL-10 and IL-22 in Mucosal Immunity: Driving Protection and Pathology. English. *Frontiers in Immunology* **11.** Publisher: Frontiers. ISSN: 1664-3224. https://www.frontiersin.org/articles/10.3389/fimmu.2020.01315/full (2021) (2020).

20. Ouyang, W. & O'Garra, A. IL-10 Family Cytokines IL-10 and IL-22: from Basic Science to Clinical Translation. en. *Immunity* **50,** 871–891. ISSN: 10747613. https://linkinghub.elsevier.com/retrieve/pii/S1074761319301372 (2021) (Apr. 2019).

21. Archer, E. J., Robinson, A. B. & Süel, G. M. Engineered E. coli That Detect and Respond to Gut Inflammation through Nitric Oxide Sensing. *ACS Synthetic Biology* **1.** Publisher: American Chemical Society, 451–457. https://doi.org/10.1021/sb3000595 (2020) (Oct. 2012).

22. Riglar, D. T. *et al.* Engineered bacteria function in the mammalian gut as long term live diagnostics of inflammation. *Nature biotechnology* **35,** 653–658. ISSN: 1087-0156. https://www.ncbi.nlm.nih.gov/pmc/articles/PMC5658125/ (2020) (July 2017).

23. Palmer, J. D. *et al.* Engineered Probiotic for the Inhibition of Salmonella via Tetrathionate-Induced Production of Microcin H47. *ACS Infectious Diseases* **4.** Publisher: American Chemical Society, 39–45. https://doi.org/10.1021/acsinfecdis.7b00114 (2020) (Jan. 2018).

24. Winter, S. E. *et al.* Gut inflammation provides a respiratory electron acceptor for Salmonella. eng. *Nature* **467,** 426–429. ISSN: 1476-4687 (Sept. 2010).

25. Wang, B., Kitney, R. I., Joly, N. & Buck, M. Engineering modular and orthogonal genetic logic gates for robust digital-like synthetic biology. en. *Nature Communications* **2.** Number: 1 Publisher: Nature Publishing Group, 508. ISSN: 2041-1723. https://www.nature.com/articles/ncomms1516 (2020) (Oct. 2011).

26. Danson, A. E., Jovanovic, M., Buck, M. & Zhang, X. Mechanisms of σ54-Dependent Transcription Initiation and Regulation. en. *Journal of Molecular Biology. RNA polymerase reaches 60* **431,** 3960–3974. ISSN: 0022-2836. http://www.sciencedirect.com/science/article/pii/S0022283619302293 (2020) (Sept. 2019).

27. Biedendieck, R. *et al.* Systems biology of recombinant protein production in Bacillus megaterium. eng. *Advances in Biochemical Engineering/Biotechnology* **120,** 133–161. ISSN: 0724-6145 (2010).

28. Kleiner-Grote, G. R. M., Risse, J. M. & Friehs, K. Secretion of recombinant proteins from E. coli. en. *Engineering in Life Sciences* **18,** 532–550. ISSN: 1618-2863. https://onlinelibrary.wiley.com/doi/abs/10.1002/elsc.201700200 (2021) (2018).

29. Chung, C. W. *et al.* Export of recombinant proteins in Escherichia coli using ABC transporter with an attached lipase ABC transporter recognition domain (LARD). *Microbial Cell Factories* **8,** 11. ISSN: 1475-2859. https://doi.org/10.1186/1475-2859-8-11 (2021) (Jan. 2009).

30. Kenny, B., Haigh, R. & Holland, I. B. Analysis of the haemolysin transport process through the secretion from Escherichia coli of PCM, CAT or beta-galactosidase fused to the Hly C-terminal signal domain. eng. *Molecular Microbiology* **5,** 2557–2568. ISSN: 0950-382X (Oct. 1991).

31. Su, L. *et al.* Extracellular overexpression of recombinant Thermobifida fusca cutinase by alpha-hemolysin secretion system in E. coli BL21(DE3). eng. *Microbial Cell Factories* **11,** 8. ISSN: 1475-2859 (Jan. 2012).

32. Linton, E., Walsh, M. K., Sims, R. C. & Miller, C. D. Translocation of green fluorescent protein by comparative analysis with multiple signal peptides. eng. *Biotechnology Journal* **7,** 667–676. ISSN: 1860-7314 (May 2012).

33. Lenders, M. H. H., Beer, T., Smits, S. H. J. & Schmitt, L. In vivo quantification of the secretion rates of the hemolysin A Type I secretion system. en. *Scientific Reports* **6.** Number: 1 Publisher: Nature Publishing Group, 33275. ISSN: 2045-2322. https://www.nature.com/articles/srep33275 (2021) (Sept. 2016).

34. Bakkes, P. J., Jenewein, S., Smits, S. H. J., Holland, I. B. & Schmitt, L. The Rate of Folding Dictates Substrate Secretion by the Escherichia coli Hemolysin Type 1 Secretion System. *The Journal of Biological Chemistry* **285,** 40573–40580. ISSN: 0021-9258. https://www.ncbi.nlm.nih.gov/pmc/articles/PMC3003356/ (2021) (Dec. 2010).

35. Ruano-Gallego, D., Fraile, S., Gutierrez, C. & Fernández, L. Á. Screening and purification of nanobodies from E. coli culture supernatants using the hemolysin secretion system. *Microbial Cell Factories* **18.** ISSN: 1475-2859. https://www.ncbi.nlm.nih.gov/pmc/articles/PMC6410518/ (2021) (Mar. 2019).

36. Schwarz, C. K. W., Landsberg, C. D., Lenders, M. H. H., Smits, S. H. J. & Schmitt, L. Using an E. coli Type 1 secretion system to secrete the mammalian, intracellular protein IFABP in its active form. eng. *Journal of Biotechnology* **159,** 155–161. ISSN: 1873-4863 (June 2012).

37. Pöhlmann, C. *et al.* Improving health from the inside. *Bioengineered* **4.** Publisher: Taylor & Francis _eprint: https://doi.org/10.4161/bioe.22646, 172–179. ISSN: 2165-5979. https://doi.org/10.4161/bioe.22646 (2021) (May 2013).

38. Rao, S. *et al.* Toward a live microbial microbicide for HIV: Commensal bacteria secreting an HIV fusion inhibitor peptide. en. *Proceedings of the National Academy of Sciences* **102,** 11993–11998. ISSN: 0027-8424, 1091-6490. http://www.pnas.org/cgi/doi/10.1073/pnas.0504881102 (2021) (Aug. 2005).

39. Hoch, J. A. Two-component and phosphorelay signal transduction. eng. *Current Opinion in Microbiology* **3,** 165–170. ISSN: 1369-5274 (Apr. 2000).

40. Merk, L. Logical Inflammation Modeling. https://github.com/lianamerk/Logical_Inflammation/tree/master.

41. Anderson, C. J. *Ribosome Binding Sites/Prokaryotic/Constitutive/Anderson* 2010. https://parts.igem.org/Ribosome%7B%5C_%7DBinding%7B%5C_%7DSites/Prokaryotic/Constitutive/Anderson.

42. Kremling, A., Heermann, R., Centler, F., Jung, K. & Gilles, E. D. Analysis of two-component signal transduction by mathematical modeling using the KdpD/KdpE system of Escherichia coli. en. *Biosystems* **78,** 23–37. ISSN: 0303-2647. http://www.sciencedirect.com/science/article/pii/S0303264704001145 (2020) (Dec. 2004).

43. Hoyle, R. B., Avitabile, D. & Kierzek, A. M. Equation-free analysis of two-component system signalling model reveals the emergence of co-existing phenotypes in the absence of multistationarity. *PLoS Comput Biol* **8,** e1002396 (2012).

44. Dayton, C. J., Prosen, D. E., Parker, K. L. & Cech, C. L. Kinetic measurements of Escherichia coli RNA polymerase association with bacteriophage T7 early promoters. en. *Journal of Biological Chemistry* **259.** Publisher: American Society for Biochemistry and Molecular Biology, 1616–1621. ISSN: 0021-9258, 1083-351X. http://www.jbc.org/content/259/3/1616 (2020) (Feb. 1984).

45. Poole, W., Pandey, A., Tuza, Z., Shur, A. & Murray, R. M. BioCRNpyler: Compiling Chemical Reaction Networks from Biomolecular Parts in Diverse Contexts. *bioRxiv* (2020).

46. Swaminathan, A., Poole, W., Hsiao, V. & Murray, R. M. Fast and flexible simulation and parameter estimation for synthetic biology using bioscrape. *bioRxiv,* 121152 (2019).

47. Halleran, A. D., Swaminathan, A. & Murray, R. M. Single Day Construction of Multigene Circuits with 3G Assembly. *ACS Synthetic Biology* **7.** Publisher: American Chemical Society, 1477–1480. https://doi.org/10.1021/acssynbio.8b00060 (2020) (May 2018).

48. Espah Borujeni, A. *et al.* Precise quantification of translation inhibition by mRNA structures that overlap with the ribosomal footprint in N-terminal coding sequences. en. *Nucleic Acids Research* **45.** Publisher: Oxford Academic, 5437–5448. ISSN: 0305-1048. https://academic.oup.com/nar/article/45/9/5437/2965383 (2020) (May 2017).

49. Meyer, A. J., Segall-Shapiro, T. H., Glassey, E., Zhang, J. & Voigt, C. A. Escherichia coli "Marionette" strains with 12 highly optimized small-molecule sensors. eng. *Nature Chemical Biology* **15,** 196–204. ISSN: 1552-4469 (2019).

50. Poole, W., Pandey, A., Shur, A., Tuza, Z. A. & Murray, R. M. BioCRNpyler: Compiling Chemical Reaction Networks from Biomolecular Parts in Diverse Contexts. *bioRxiv.* eprint: https://www.biorxiv.org/content/early/2020/08/03/2020.08.02.233478.full.pdf. https://www.biorxiv.org/content/early/2020/08/03/2020.08.02.233478 (2020).

51. Tzschaschel, B. D., Guzmán, C. A., Timmis, K. N. & Lorenzo, V. d. An Escherichia coli hemolysin transport system-based vector for the export of polypeptides: Export of shiga-like toxin IIeB subunit by Salmonella typhimurium aroA. en. *Nature Biotechnology* **14.** Number: 6 Publisher: Nature Publishing Group, 765–769. ISSN: 1546-1696. https://www.nature.com/articles/nbt0696-765 (2021) (June 1996).

52. Der, B. S. *et al.* DNAplotlib: Programmable Visualization of Genetic Designs and Associated Data. *ACS Synthetic Biology* **6.** Publisher: American Chemical Society, 1115–1119. https://doi.org/10.1021/acssynbio.6b00252 (2020) (July 2017).

53. Pöhlmann, C. *et al.* Periplasmic delivery of biologically active human interleukin-10 in Escherichia coli via a sec-dependent signal peptide. eng. *Journal of Molecular Microbiology and Biotechnology* **22,** 1–9. ISSN: 1660-2412 (2012).

54. Lin, Y., Krogh-Andersen, K., Hammarström, L. & Marcotte, H. Lactobacillus delivery of bioactive interleukin-22. *Microbial Cell Factories* **16,** 148. ISSN: 1475-2859. https://doi.org/10.1186/s12934-017-0762-1 (2021) (Aug. 2017).

55. Crook, N. *et al.* Adaptive Strategies of the Candidate Probiotic E. coli Nissle in the Mammalian Gut. en. *Cell Host & Microbe* **25,** 499–512.e8. ISSN: 1931-3128. http://www.sciencedirect.com/science/article/pii/S1931312819301015 (2020) (Apr. 2019).

56. Merk, L. N., Shur, A. S., Pandey, A., Murray, R. M. & Green, L. N. Engineering Logical Inflammation Sensing Circuit for Gut Modulation. en. *bioRxiv.* Publisher: Cold Spring Harbor Laboratory Section: New Results, 2020.11.10.377085. https://www.biorxiv.org/content/10.1101/2020.11.10.377085v1 (2021) (Nov. 2020).